Distinct functions of the kinesin-9 family in mammalian motile cilia

Chuyu Fang[1,2,†], Xinwen Pan[1,3,†], Di Li[4,†], Yawen Chen[1,2], Luan Li[1,2], Qi Gao[1,2], Dong Li[4,*], Xueliang Zhu[1,2,3,5,*] and Xiumin Yan[6,*]

[1] State Key Laboratory of Cell Biology, Shanghai Institute of Biochemistry and Cell Biology, Center for Excellence in Molecular Cell Science, Chinese Academy of Sciences, 320 Yueyang Road, Shanghai 200031, China

[2] University of Chinese Academy of Sciences, Beijing 100049, China

[3] School of Life Science and Technology, ShanghaiTech University, China

[4] National Laboratory of Biomacromolecules, CAS Center for Excellence in Biomacromolecules, Institute of Biophysics, Chinese Academy of Sciences, Beijing, China

[5] School of Life Science, Hangzhou Institute for Advanced Study, University of Chinese Academy of Sciences, Hangzhou 310024, China

[6] Ministry of Education-Shanghai Key Laboratory of Children's Environmental Health, Xinhua Hospital, Shanghai Jiao Tong University School of Medicine, Shanghai 200092, China

[†] Co-first author

* Corresponding author (e-mail: lidong@ibp.ac.cn, xlzhu@sibcb.ac.cn or yanx@shsmu.edu.cn)

Abstract

Motile cilia, with 9+2 axonemes, propel directional fluid flows by coordinated beating for various physiological functions. The kinesin-9 family comprises Kif6 and Kif9, known for their involvement in regulating flagella motility across species. However, the precise roles of mammalian kinesin-9 family remain unclear. In this study, we reveal the distinct localizations and functions of Kif6 and Kif9 in mammalian motile cilia. Kif6 associates with intraflagellar transport (IFT) particles and exhibits bidirectional movements within motile cilia. Knockout of *Kif6* results in severe hydrocephalus due to impaired planar polarity and directional fluid flow in the ependyma. Conversely, Kif9 localizes to the axonemal central lumen, and its depletion causes brain ventricular expansion and defective sperm motility. These findings shed light on the diverse functions of the kinesin-9 family in motile cilia and flagella, providing valuable insights into the complex regulatory mechanisms underlying ciliary trafficking and motility.

Keywords

Kinesin; intraflagellar transport; ependymal cells; ciliary motility; planar cell polarity; Kif6; Kif9; hydrocephalus; basal body

Introduction

Cilia are evolutionarily conserved, microtubule (MT)-based organelles that protrude from the cell surface and are generally categorized into primary and motile cilia (Klena and Pigino, 2022). Primary cilia, with a 9+0 MT arrangement, are present in most mammalian cell types and serve as an 'antenna' to sense environmental cues such as mechanical, chemical, and light signals (Goetz and Anderson, 2010; Nachury and Mick, 2019). On the other hand, motile cilia/flagella typically possess a 9+2 MT axoneme with a central pair (CP) of MT singlets (C1 and C2) surrounded by peripheral nine doublet MTs (DMTs) (Klena and Pigino, 2022). The CP MTs are decorated with proteinaceous projections and the peripheral DMTs are equipped with dynein arms and radial spokes. The signal from CP apparatus transmits through radial spokes to govern the sliding of axonemal dyneins along adjacent MTs, generating cilia/flagella beating(Hoek et al., 2022; Lechtreck et al., 2009). With the exception of sperm flagella, motile cilia are mainly present as multicilia with dozens to hundreds of cilia within a single cell in mammals. Multicilia are found in epithelia of various organs such as the brain ventricles, the airway and the oviduct, playing critical roles in cerebrospinal fluid (CSF) circulation, mucus clearance, and ovum transport (Marshall and Kintner, 2008; Ohata and Alvarez-Buylla, 2016).

To generate directional fluid flow, proper polarities are needed to establish at both cellular and tissue levels. During the differentiation of multiciliated cells, basal bodies (BBs) initially amplify and dock randomly to the cell membrane, as indicated by the orientiation of their basal feet (BFs), which align with the direction of effective strokes (Gibbons, 1961; Guirao et al., 2010; Ohata and Alvarez-Buylla, 2016). As maturation progress, the orientation of BBs within individual cells gradually aligns in a coordinated manner along the direction of fluid flow, establishing rotational polarity (Boutin et al., 2014; Guirao et al., 2010; Werner et al., 2011). In ependymal cells, in addition to rotational polarity, BBs exhibit a specific clustering into a patch on one side of the cell surface, establishing translational polarity that distinguishes them from other multiciliated cells such as tracheal epithelial cells (Mirzadeh et

al., 2010). These processes ultimately establish the planar polarity of multiciliated tissues. The establishment of planar polarity involves planar cell polarity (PCP) pathway and hydrodynamic force flow, guiding the process over several days (Boutin et al., 2014; Guirao et al., 2010; Ohata and Alvarez-Buylla, 2016).

Kinesins are motor proteins that play essential roles in directional transport of cargos along MTs and regulation of MT dynamics in various cellular processes such as mitosis, ciliogenesis and intracellular transport across eukaryotes (Cason and Holzbaur, 2022; Hirokawa et al., 2009). They are classified into N-kinesins, M-kinesins, and C-kinesins based on the position of motor domain. Two kinesin families, kinesin-2 and 9, have been found to function in cilia or flagella. Among them, the kinesin-2 family motors (Kif3a/b/c) are well-known for their involvement in IFT, a specialized bidirectional transportation machinery (Bhogaraju et al., 2013; Scholey, 2013; Taschner et al., 2016; Zhao et al., 2012). IFT relies on two multi-subunit complexes, IFT-A and IFT-B, which are powered by kinesin-2 or cytoplasmic dynein-2 respectively for anterograde or retrograde trafficking along the axonemal MTs. This process enables the transport of ciliary proteins in and out of cilia, critical for cilia assembly, maintenance, and function (Jordan et al., 2018; Klena and Pigino, 2022; Meleppattu et al., 2022; Pazour et al., 1998; Pigino, 2021).

The kinesin-9 family consists of two members, Kif6 and Kif9, which share a high sequence identity at their motor domains. They belong to the N-kinesin group, typically involved in plus-end-directed transports of cargos. Unlike the kinesin-2 family, which plays a critical role in both primary and motile cilia, the kinesin-9 family is predominantly associated with flagellated species (Demonchy et al., 2009), suggesting distinct or redundant roles in regulating flagella motility. In *Chlamydomonas*, only KLP1, the homolog of Kif9, has been studied. It specifically localizes to the CP MTs and is proposed as an active motor to regulate flagellar motility (Bernstein et al., 1994; Han et al., 2022; Yokoyama et al., 2004). Interestingly, in *Trypanosoma*, the kinesin-9 family has been demonstrated distinct functions in flagella motility (Demonchy et al., 2009). Depletion of *KIF9A*, the *Trypanosoma* homolog of *Kif9*, reduces flagellum beating and cell movement, while knockdown of *KIF9B*, the

homolog of *Kif6*, results in cell paralysis and defective assembly of the paraflagellar rod (PFR). The PFR, a unique large structure found exclusively in euglenoids and kinetoplastids, is asymmetrically attached to the axoneme at DMTs 4-7, critical for flagella beating and cell locomotion (Demonchy et al., 2009; Portman and Gull, 2010; Zhang et al., 2021). Although there is no observed movement of KIF9B within flagella, it is speculated that KIF9B is involved in PFR transport or the recognition of axoneme asymmetry for PFR assembly in *Trypanosoma* (Demonchy et al., 2009). This raises the question of whether Kif6, in other species, also contributes to ciliary trafficking of essential materials involved in cilia beating and recognition or establishment of axonemal polarity. In mammals, mutations in *Kif9* have been associated with defective sperm motility and impaired fertility (Meng et al., 2022; Miyata et al., 2020). A frameshift mutation of *KIF6* has been found in a patient with intellectual disability and megalocephaly (Buchan et al., 2014; Konjikusic et al., 2018). Mice carrying a *Kif6* C-terminal truncation mutant (*Kif6*$^{p.G555fs}$) develop severe hydrocephalus possibly due to defective ciliogenesis in the ependyma (Buchan et al., 2014; Konjikusic et al., 2018). Despite these achievements, a comprehensive understanding of the roles of Kif6 and Kif9 in mammalian ciliary trafficking and cilia motility is still lacking.

In this study, we investigate the functions of Kif6 and Kif9 in mice. Kif6 is a motile-cilia specific kinesin and plays a critical role in ciliary transportation, essential for the establishment of planar polarization in the ependyma, while Kif9 likely functions within the CP projection for the regulation of motile cilia/flagella motility.

Results

Mammalian Kif6 and Kif9 are motile cilia-specific kinesins with distinct localizations

Murine full-length Kif6 (NP_796026.2) and Kif9 (NP_001157041.1) are highly conserved proteins composed of 802 and 810 amino acid residues, respectively. Structurally, both proteins have a motor domain located at the N-terminus, followed by two coiled-coil regions and a tail at the C-terminus (Fig. 1a) (Hirokawa et al., 2009; Miki et al., 2005). The motor domains of the two proteins share ~43% sequence identity, while their C-terminus are less conserved (Fig.1a and Supplementary Fig. 1a, b) (Miki et al., 2005). Phylogenetic

122 analysis showed Kif6 and Kif9 co-existed in eukaryotes with motile cilia/flagella, dating back
123 to protists like *Chlamydomonas* (Fig. 1b and Supplementary Fig. 1b) (Bernstein et al., 1994;
124 Vincensini et al., 2011; Yokoyama et al., 2004). In constrast, Kif6 and Kif9 homologues are
125 absent in *Caenorhabditis elegans* which only contain immotile sensory cilia (Fig. 1b) (Inglis
126 et al., 2007; Vincensini et al., 2011). These data suggest that Kif6 and Kif9 may have
127 important roles not only in flagella but also in motile cilia.

128 Analysis on our previous microarray results (Xu et al., 2015) demonstrated that *Kif6* and
129 *Kif9* were highly upregulated during the multiciliation of mouse tracheal epithelial cells
130 (mTECs) (Fig. 1c). Immunoblots confirmed a substantial increase in the protein levels of Kif6
131 and Kif9 during multiciliation of mTECs (Fig. 1d). Furthermore, Kif6 and Kif9 were
132 specifically expressed in tissues and cells abundant in motile cilia, such as the ependyma, the
133 trachea, the lung, the testis, and primary cultured mouse ependymal cells (mEPCs), but were
134 hardly detected in primary ciliated tissues and cells (Fig. 1e, f) (Duan et al., 2021; Fliegauf et
135 al., 2007). To visualize their subcellular localizations, we immunostained mEPCs and IMCD3
136 cells with antibodies against Kif6 or Kif9 (Fig. 1g-i). Confocal analysis revealed that both
137 Kif6 and Kif9 localized to the axoneme of motile cilia in mEPCs (Fig. 1h), but not to the
138 axoneme of primary cilia in IMCD3 cells (Fig. 1i). To validate their ciliary localization, we
139 infected mEPCs with adenovirus to express Kif6-GFP or Kif9-GFP (Fig. 1g, j). Consistently,
140 Kif6-GFP and Kif9-GFP were clearly observed in ciliary axonemes of mEPCs (Fig. 1j).

141 Super-resolution microscopy analysis revealed that ciliary Kif9 was distributed at the CP
142 region, when Hydin, a C2 projection protein (Lechtreck et al., 2008), and acetylated tubulin
143 (Ac-tub) were respecitively used as CP and axoneme markers (Fig. 1k), suggesting a
144 conserved localization in the C2 projection as *Chlamydomonas* KLP1 (Han et al., 2022). In
145 sharp contrast, Kif6 localized along the axonemes as puncta (Fig. 1l). Similar ciliary
146 localization patterns were observed when GFP-tagged Kif6 and Kif9 were expressed in
147 mEPCs and co-immunostained with Spef1, another CP protein (Supplementary Fig. 2a, b)
148 (Zheng et al., 2019).

Collectively, our results demonstrate the specific localization of Kif6 and Kif9 within motile cilia. Kif6 localizes as punta along the peripheral DMTs of axonemes, whereas Kif9 is specifically enriched in the CP lumen. Their distinct localization patterns imply potential unique roles for the two kinesins in mammalian motile cilia.

Kif6, but not Kif9, moves along ciliary axoneme and colocalizes with IFT particles

As kinesins with a motor domain at their N-terminus typically function as plus-end-directed motor proteins (Cason and Holzbaur, 2022; Hirokawa et al., 2009), we examined whether Kif6 and Kif9 could move along DMTs and central MTs, respectively. We employed the high spatiotemporal resolution, grazing incidence structured illumination microscopy (GI-SIM) (Guo et al., 2018; Qiao et al., 2022) to record the movements of GFP-tagged Kif6 and Kif9 in mEPCs (Fig. 2a-e and Movies 1-3). In these experiments, we used one IFT-B component Ift81-GFP as a positive control (Kanie et al., 2017). Immunoblotting demonstrated a comparable expression level of Kif6-GFP and Ift81-GFP with their endogenous proteins, while Kif9-GFP showed higher expression than endogenous Kif9 (Fig. 2b). As expected, Ift81-GFP particles displayed clear bidirectional movements along the axonemes (Fig. 2c and Supplementary Fig. 3a, top; Movie 1). Strikingly, Kif6-GFP particles also underwent robust and processive movements in both the anterograde and retrograde directions along the axonemes, resembling the movement of Ift81-GFP particles (Fig. 2d and Supplementary Fig. 3a, middle; Movie 2). In contrast, we did not detect any processive movement of Kif9-GFP along the entire axonemes (150 cilia from 10 cells) (Fig. 2e and Supplementary Fig. 3a, bottom; Movie 3).

Qunatification results revealed that Ift81-GFP moved at velocities of 0.73 ± 0.40 μm/s for anterograde and 0.67 ± 0.36 μm/s for retrograde (Fig. 2f). The velocities were slightly faster than the IFT in primary ciliated IMCD3 cells and the olfactory sensory neurons but slower than those in *C. elegans* and *Chlamydomonas* (Williams et al., 2014; Wingfield et al., 2017). Kif6-GFP labeled puncta moved at similar velocities to Ift81-GFP, with the mean velocities of 0.71 ± 0.34 μm/s for anterograde and 0.64 ± 0.34 μm/s for retrograde (Fig. 2f)

176 transports. The frequency of anterograde movement for Kif6-GFP particles (13.3 ± 11.3
177 counts/min) was similar to that of Ift81-GFP particles (14.0 ± 10.0 counts/min). However, the
178 retrograde frequency of Kif6-GFP puncta appeared slightly decreased compared to Ift81-GFP
179 particles (11.0 ± 9.0 vs 13.2 ± 9.9 counts/min) (Fig. 2g), suggesting that a portion of Kif6 may
180 diffuse back to the ciliary base like kinesin-2 after it reached to ciliary tip (Chien et al., 2017).
181 Since Kif6 exhibited comparable velocity and frequency characteristics to those of IFT
182 particles, we expressed Kif6-GFP in mEPCs and co-immunostained with antibodies against
183 two components of IFT-B complexes (Ift56 and Ift88) to further explore their relationship
184 (Kanie et al., 2017; Taschner et al., 2014). Confocal imaging unveiled a notable colocalization
185 between Ift56 and Kif6-GFP at the axoneme (Fig. 2h). Three-dimensional structured
186 illumination microscopy (3D-SIM) images further showed their punctate colocalization along
187 the axonemal DMTs (Fig. 2i). Similar results were observed when Kif6-GFP was co-
188 immunostained with Ift88 (Supplementary Fig. 3b, c).
189 Taken together, our findings demonstrate the bidirectional movements of Kif6 within
190 motile cilia, which is not observed for Kif9. The similarity in movement behaviors,
191 velocitities and frequencies between Kif6 and IFT particles strongly suggest a potential
192 involvement of Kif6 in IFT trafficking.
193 **Kif6-GFP puncta exhibit comovement with IFT particles along axonemal MTs**
194 To gain further insights into the relationship between Kif6 and IFT particles, we co-
195 expressed Kif6-GFP and Ift27-Halo, another IFT-B component (Kanie et al., 2017), in
196 mEPCs by adenoviral infection and performed dual-color time-lapse GI-SIM imaging (Fig.
197 3). Before imaging, a calibration of the microscope was performed routinely with fluorescent
198 beads, ensuring that different fluorescent channels were acculartely aligned in GI-SIM
199 (Supplementary Fig. 3d). Interestingly, we observed three distinct bidirectional moving
200 particles within cilia: particles labeled with both Ift27-Halo and Kif6-GFP ($Ift27^{+}Kif6^{+}$
201 particles), those labeled only with Kif6-GFP ($Kif6^{+}$ particles), and those labeled only with
202 Ift27-Halo ($Ift27^{+}$ particles) (Fig. 3a-c; Movies 4-5). The corresponding komographs
203 confirmed the presence of these three types of particles (Fig. 3a-c and Movies 4-5). The ratio

204 of these three trafficking types were approximately 1:1.5:1 ($Ift27^+Kif6^+$:$Kif6^+$:$Ift27^+$) in both
205 anterograde and retrograde directions (45 cilia in total from 4 cells) (Fig. 3d). These particle
206 types exhibited similar velocities for both anterograde and retrograde transports (Fig. 3e and
207 Movies 4-5). Specifically, $Ift27^+$ particles showed velocities of 0.70 ± 0.31 μm/s for
208 anterograde and 0.62 ± 0.28 μm/s for retrograde transport. $Kif6^+$ particles moved at velocities
209 of 0.74 ± 0.32 μm/s and 0.65 ± 0.34 μm/s, respectively. $Ift27^+Kif6^+$ particles moved at
210 velocities of 0.75 ± 0.32 μm/s and 0.66 ± 0.28 μm/s, respectively (Fig. 3e).

211 Taken together, the distribution of Kif6 observed in fixed samples and time-lapse
212 experiments indicate that Kif6, unlike Kif9, is not a structural component of motile cilia,
213 functions as an active motor in ciliary trafficking. The presence of IFT-free Kif6 particles
214 suggests independent movements of Kif6 along the cilia.

215 **Mice lacking *Kif6* or *Kif9* develop hydrocephalus and exhibit male infertility**

216 Function of Kif6 has been explored using *Kif6*$^{p.G555fs}$ mice which develop severe
217 hydrocephalus (Konjikusic et al., 2018). Since the mutant mice still express the motor domain
218 of Kif6, the observed hydrocephalus phenotype could be caused by the dominant negative
219 effect of the remaining motor domain. Additionally, depletion of *Kif9* results in defective
220 sperm motility in mice, with its function in motile cilia remaining unexplored (Miyata et al.,
221 2020). To uncover their physiological function *in vivo* and the mechanism involved, we
222 generated *Kif6* and *Kif9* knockout mice (Fig. 4a, b) using the CRISPR/Cas9 system (Joung et
223 al., 2017). Immunoblotting confirmed complete depletion of Kif6 or Kif9 (Fig. 4c). Both *Kif6*$^{-}$
224 $^{/-}$ and *Kif9*$^{-/-}$ mice were born at the expected Mendelian ratio of genotypes. The majority of
225 *Kif6*$^{-/-}$ mice experienced growth failure and often exhibited a dome-shaped skull compared to
226 wild-type littermates after P21, suggestive of severe hydrocephalus (Fig. 4d, indicated by
227 arrows). Some of these mice displayed more pronounced cranial deformities and skull
228 expansion, leading to a forward rounding of the back or kyphosis with a smaller stature
229 compared to their littermates (Fig. 4d, indicated by arrowhead). Careful examination of brain
230 dissections or coronal sections revealed that every analyzed *Kif6*$^{-/-}$ mouse (100%; total n = 60)

displayed lateral ventricle expansion when compared to the wild-type controls (Fig. 4f, h). This ventricle enlargement was evident even in mice that displayed a normal skull appearance and longer lifespan (Fig. 4f, bottom). In sharp contrast to *Kif6*$^{-/-}$ mice, *Kif9*$^{-/-}$ mice appeared normal similar to their wild-type littermates based on macroscopic examination (Fig. 4e). However, coronal brain sections revealed enlarged ventricles in over half of *Kif9*$^{-/-}$ mice (Fig. 4g, h), indicative of hydrocephalus. Survival curve analysis revealed that approximately 77% of *Kif6*$^{-/-}$ mice died before reaching P90, while *Kif9*$^{-/-}$ mice exhibited a normal lifespan similar to their wild-type littermates during a 12-month observation period (Fig. 4i).

We did not observed noticeable defects in organs where primary cilia are critical, such as polydactyly or polycystic kidney (Duan et al., 2021; Fliegauf et al., 2007), suggesting that primary cilia might not be affected. Consistent with the previous study, although *Kif9*$^{-/-}$ male mice displayed a normal sperm count. However, there was a decline in sperm motility and poor male fertility (Movie 6), similar to previous observation (Miyata et al., 2020). Contrarily, *Kif6*$^{-/-}$ mice that reached reproductive age (~ 2 months) showed a significant reduction in sperm count. Notably, while the sperm of *Kif6*-deficiency mice had normal morphology, they exhibited almost no motility (Fig. 4j, k and Movie 7). These observations emphasize the critical but distinct roles of Kif6 and Kif9 in motile cilia and sperm flagella.

Kif6 but not _Kif9_ deficiency disrupts the planar polarity of ependymal motile cilia

Ependymal multiciliated cells are responsible for generating unidirectional CSF flow through planar-polarized cilia beating in the brain ventricle (Marshall and Kintner, 2008; Ohata and Alvarez-Buylla, 2016). Abnormalities in cilia formation and motility of ependymal cells cause hydrocephalus (Matsuo et al., 2013; Mirzadeh et al., 2010; Tissir et al., 2010). Given that the knockout of *Kif6* and *Kif9* resulted in hydrocephalus, we thus assessed the impact of Kif6 and Kif9 on ciliogenesis and cilia motility (Fig. 5a). As Kif6 was found to be associated with IFT in ependymal cilia, we firstly employed scanning electron microscopy (SEM) to determine if Kif6 is required for ciliogenesis. We examined whole-mounts of ependyma from *Kif6*$^{-/-}$ mice and their wild-type littermates at P4, the time of cilia formation (Spassky et al., 2005). Our SEM analysis revealed that both the number and morphology of

259 cilia in ependymal cells remained unaffected by *Kif6* deficiency (Fig. 5b, top). Simliar
260 observations were obtained when using mice at P30 (Fig. 5b, bottom), implying that depletion
261 of *Kif6* does not affect ciliogenesis, different from the defective ciliogenesis observed in
262 *Kif6*$^{p.G555fs}$ mice (Konjikusic et al., 2018). Moreover, transmission electron microscopy (TEM)
263 exhibited no discernible ultrastructure abnormalities in the ciliary axoneme of *Kif6*-deficient
264 mice (Supplementary Fig. 4a).

265 As ependymal cells display unidirectional beating at tissue level after P21 (Guirao et al.,
266 2010; Ohata and Alvarez-Buylla, 2016), to assess the effect of *Kif6* or *Kif9* knockout on
267 ciliary motility, we labeled the lateral ventricles derived from mice after P21 with SiR-
268 tubulin, a live-cell microtubule fluorescent probe (Lukinavicius et al., 2014) and conducted
269 live-cell imaging using high-speed spinning disk confocal microscopy (Fig. 5a). A ciliary beat
270 cycle typically consists of a quick effective stroke and a slower recovery stroke (Lechtreck et
271 al., 2009). To clarify the ciliary beat pattern, we traced and analyzed the movement of cilia
272 from both side and top views. Strikingly, we observed that cilia in individual *Kif6*$^{-/-}$
273 ependymal cells, regardless of the severity of hydrocephalus, exhibited metachronal
274 synchrony, beating in a back-and-forth asymmetric manner, resembling the behavior seen in
275 wild-type littermates (Fig. 5c and Supplementary Fig. 4b). Notably, the ciliary beat
276 frequencies of *Kif6*$^{-/-}$ cilia (23.4 ± 6.3 Hz) were similar to those of wild-type counterparts
277 (23.9 ± 6.4 Hz) (Fig. 5d). In contrast, at the tissue level, wild-type ependymal cells exhibited
278 metachronal coordination, predominantly beating in one direction (Fig. 6e and Supplementary
279 Fig. 4c; Movie 8). However, the coordination of ciliary beat directions within *Kif6*$^{-/-}$
280 ependyma was significantly disrupted (Fig. 5e and Supplementary Fig. 4c; Movie 9),
281 indicating impaired PCP (Mirzadeh et al., 2010; Ohata and Alvarez-Buylla, 2016).

282 Similar to the loss of *Kif6*, depletion of *Kif9* did not significantly alter the number and
283 length of cilia. Additionally, individual ependymal cells from *Kif9*$^{-/-}$ littermates exhibited
284 well-coordinated, asymmetric beating patterns (Fig. 5f and Supplementary Fig. 4d). In
285 contrast to *Kif6*$^{-/-}$ ependyma (Fig. 5e and Supplementary Fig. 4c; Movie 9), multicilia in *Kif9*$^{-/-}$
286 ependyma displayed metachronal coordination at the tissue level, resembling the wild-type

287 controls (Fig. 5g and Supplementary Fig. 4e; Movies 10-11). Moveover, cilia beat frequencies
288 in *Kif9*$^{-/-}$ ependymal cilia remained unchanged compared to wild-type controls
289 (Supplementary Fig. 4f).

290 Given that the knockout of *Kif6* resulted in uncoordinated ciliary beating across the
291 ependyma (Fig. 5h, i), we performed a beads assay to investigate whether disrupted cilia
292 beating in *Kif6*$^{-/-}$ mice leads to impaired fluid flow, ultimately contributing to the development
293 of hydrocephalus. Latex fluorescent microbeads were added to freshly prepared brain slices
294 and their movements were tracked to quantitatively assess dynamic fluid flow. In wide-type
295 samples, the beads displayed a relatively uniform drift in one direction (Fig. 5h; Movie 12).
296 Conversely, in *Kif6*$^{-/-}$ samples, the uncoordinated cilia beats mainly drove the beads to
297 oscillate or whirl regionally (Fig. 5h; Movie 13). The velocities of beads in *Kif6*$^{-/-}$ mice were
298 46.3 ± 15.4 μm/s slower than those in wild-type mice (63.6 ± 27.1 μm/s) (Fig. 5i).

299 Taken together, our results suggest that the loss of *Kif6* and *Kif9* does not affect
300 ciliogenesis. However, the absence of *Kif6*, but not *Kif9*, does impair the coodinated ciliary
301 beats at tissue-level which may contribute to the development of hydrocephalus.

302 **Kif6 is crucial for the establishment of rotational polarity of BBs in ependymal tissues**

303 Since the coordiated cilia beating closely relates with the orientation of BBs (Mirzadeh et
304 al., 2010; Ohata and Alvarez-Buylla, 2016), we examined the BB polarity in both *Kif6*$^{-/-}$ and
305 *Kif9*$^{-/-}$ ependyma. We immunostained whole-mounts of ependyma from wild type, *Kif6*$^{-/-}$ and
306 *Kif9*$^{-/-}$ mice using Cep164, a transition fiber component (Graser et al., 2007; Siller et al.,
307 2017), to mark BBs, and γ-tubulin or Centriolin to label BFs (Fig. 6a-e and Supplementary
308 Fig. 5) (Nguyen et al., 2020; Ohata et al., 2014). 3D-SIM images revealed a uniform
309 rotational polarity of BB patches and consistent tissue-level polarity in both wild type and
310 *Kif9*$^{-/-}$ wholemounts (Fig. 6b, c and Supplementary Fig. 5a, b). In contrast, both the rotational
311 and tissue polarity of BBs were markedly impaired in *Kif6*-deficient ependyma, regardless of
312 the severity of hydrocephalus (Fig. 6d, e and Supplemenatry Fig. 5c, d). To assess the extent
313 of the rotational polarity in individual cells, we measured the mean vector length by
314 considering each arrow marking the BF orientation as a unit vector (Bustamante-Marin et al.,

315 2019; Werner et al., 2011). As expected, our analysis revealed that the mean vector length of
316 BBs in wild-type and *Kif9*$^{-/-}$ ependymal cells was close to 1 (0.95 ± 0.03 for wild type; 0.95 ±
317 0.04 for *Kif9*$^{-/-}$) (Fig. 6f). In contrast, the mean vector length of BBs was significantly reduced
318 in *Kif6*$^{-/-}$ samples (0.32 ± 0.15 for mice with mild hydrocephalus; 0.28 ± 0.14 for mice with
319 severe hydrocephalus) (Fig. 6f), suggesting an impaired rotational polarity of BBs. Similar
320 quantitative results were obtained when used Centriolin as the BF marker (Supplementary
321 Fig. 5e). TEM images further confirmed the proper alignment of BFs in wild-type ependyma
322 (mean vector length = 0.97 ± 0.07) and the impaired rotational polarity of BBs in *Kif6*$^{-/-}$
323 ependyma, in both mild (0.35 ± 0.17) and severe (0.31 ± 0.18) hydrocephalus mice (Fig. 6g,
324 h). Our results highlight the crucial role of Kif6, rather than Kif9, in the establishment of
325 rotational polarity of BBs in ependyma, essential for coordinated cilia beating at the tissue
326 level (Fig. 6i).

327 In contrast to the rotational polarity, BB patches displayed conspicuous asymmetric
328 distributions within the cells of both mild and severe hydrocephalus *Kif6*$^{-/-}$ mice
329 (Supplementary Fig. 6a-c). The area of BB patches also remained unaffected in *Kif6*$^{-/-}$ mice
330 with a mild hydrocephalus, however, we did observe a slight increase in the BB patches area
331 in samples with severe hydrocephalus (Supplementary Fig. 6d), potentially influenced by the
332 pathological effects of hydrocephalus, suggesting that Kif6 may be dispensable for
333 translational polarity (Ohata and Alvarez-Buylla, 2016). Notably, the depletion of *Kif6* and
334 *Kif9* did not affect the number of BBs (Fig. 6j), consistent with unaffected ciliogenesis (Fig.
335 5b, e, g and Supplementary Fig. 4c, e).

336 **Discussion**

337 In this study, we show that Kif6 and Kif9, two kinesin-9 family members, have unique
338 ciliary localizations and functions in mammalian motile cilia and flagella (Fig. 1b and 6k).
339 Kif9 is mainly found in the CP lumen in motile cilia, while Kif6 localizes along the DMTs
340 and can move bidirectionally along the ciliary axoneme (Fig. 1-3 and Supplementary Fig. 3).
341 In knockout mice, neither Kif6 nor Kif9 are necessary for ciliogenesis (Fig. 5 and

Supplementary Fig. 4). Specifically, *Kif6* knockout leads to reduced sperm motility (Fig. 4k and Movie 7) and disrupted cilia motility coordination (Fig. 5e and Supplementary Fig. 4c; Movie 9), causing hydrocephalus (Fig. 3d, f, h) and male infertility. Interestingly, *Kif6* depletion causes flagella paralysis in *Trypanosoma* (Demonchy et al., 2009) and impairs sperm flagella motility in mice (Fig. 4k and Movie 7), but it does not impact the beating frequency of motile cilia (Fig. 5d). *Kif9* knockout affects flagella motility with minimal impact on motile cilia (Fig. 5 and Supplementary Fig. 4; Movie 6). These differences suggest distinct regulatory mechanisms, potentially linked to different beating patterns like the back-and-forth pattern of ependymal cilia, and the non-planar waveform pattern of sperm flagella (Gadadhar et al., 2021; Lechtreck et al., 2009; Miyata et al., 2020).

The kinesin-9 family belong to N-kinesins, usually facilitate plus-end-directed cargo transports (Cason and Holzbaur, 2022; Demonchy et al., 2009). Using GI-SIM, we find that Kif6 but not Kif9 undergoes processive movement in ependymal cilia (Figs. 2-3 and Supplementary Fig. 3; Movies 2-4). The result of mammalian Kif9 is consistent with the observation in *Xenopus* epidermal multiciliated cells (Konjikusic et al., 2023), suggesting that Kif9 is not involved in the ciliay transport along the cilia. Considering the conserved CP localization of Kif9 and brain ventricle expansion phenotype observed in over half of *Kif9*$^{-/-}$ mice (Fig. 4g, h), Kif9 may regulate ependymal cilia beating, potentially mediating conformation changes of CP MTs during beating. Future studies such as cryo-electron tomography technology (Cryo-ET) studies will be needed to investigate this hypothesis. Most strikingly, we observe the bidirectional movement of Kif6 along the ciliary axoneme and association of IFT particles (Figs. 2, 3 and and Supplementary Fig. 3). Although Kif6 is not essential for ciliogenesis (Fig. 4 and Supplementary Fig. 4), it is the only known kinesin specifically involved in the IFT process within motile cilia. Its co-movement with IFT particles suggests Kif6 may serve as a cargo adaptor or as an active motor contributing to the delivery of proteins critical for establishing planar polarity (Fig. 6k). Further investigations are required to confirm this.

Kif6 deficiency does not affect translational polarity of BBs, but it does disrupt the

370 rotational polarity of BBs and planar polarity of cilia in ependyma (Figs. 5-7 and
371 Supplementary Figs. 4-5; Movie 9). Since PCP pathway is key for translational polarity
372 (Mirzadeh et al., 2010; Ohata and Alvarez-Buylla, 2016), Kif6 likely does not function
373 upstream of the PCP pathway. Instead, it may transport specific cargos like signalling
374 molecules within motile cilia that respond to hydrodynamic forces or downstream of PCP
375 signaling (Fig. 6k). This idea is supported by the misalignment of BBs in *Kif6*$^{-/-}$ mice, similar
376 to obervations in cultured mEPCs lacking external flow force (Guirao et al., 2010).
377 Furthermore, this speculation is also supported by *Kif6*$^{-/-}$ mice not showing obvious airway
378 defects, where the rotational polarity of BBs could align properly without flow forces *in vitro*
379 (Herawati et al., 2016). In *Trypanosoma*, the absence of *KIF9B*, a *Kif6* homolog, disrupts the
380 assembly of the PFR, a structure asymmetrically assembled at DMTs 4-7 along the flagellar
381 axoneme, required for flagella motility (Demonchy et al., 2009; Zhang et al., 2021).
382 Interestingly, in mammals, "9+2"-type motile cilia also exhibit an asymmetric axonemal
383 orientation. For instance, the CP plane is perpendicular to the direction of ciliary beat, and the
384 direction of BFs aligns with the effective stroke of cilia (Butler and Wallingford, 2017; Clare
385 et al., 2014; Lindemann and Lesich, 2021; Ohata and Alvarez-Buylla, 2016). The disturbance
386 of the rotational polarity of BBs in *Kif6*$^{-/-}$ ependymal cells suggests a role of Kif6 to help
387 ensure proper axonemal asymmetry and BB polarity. Notably, *Kif6*$^{-/-}$ sperm flagella are nearly
388 immobile, resembling the *KIF9B*-defective *Trypanosoma* flagella. As sperm flagella have
389 multiple extra-axonemal structures, further research into function of Kif6 in these structures
390 could provide interesting insights.
391 In summary, our findings from *Kif6* and *Kif9* knockout mice and GI-SIM experiments
392 have elucidated the crucial role of Kif6 in BB polarization and its necessity for coordinated
393 cilia beating, potentially through its involvement in motile cilia-specific transport.
394 Furthermore, bidirectional trafficking of Kif6 suggests that it may deliver materials critical for
395 coordinated cilia beating across ependymal tissues. Some Kif6 puncta appear independent of
396 IFT particles, hinting at separate protein transport from IFT, though further investigation is
397 needed. Identifying molecules or substructures associated with Kif6 could provide more

398 insight into the regulatory mechanism. Although *Kif9* depletion does not significantly impact
399 ciliary motility, its role in sperm motility and brain ventricle expansion suggests a critical
400 function in flagella/motile cilia motility.

401 Methods

402 Plasmids

403 The cDNAs encoding full-length *Kif6* (GenBank: NM_177052.3), *Kif9* (GenBank:
404 NM_001163569.1), *Ift81* (GenBank: NM_001358917.1), and *Ift27* (GenBank:
405 NM_025931.3) were amplified using PCR with cDNAs extracted from cultured mEPCs (Day
406 10) as the template. To generate adenoviral expression constructs, the cDNAs fragments were
407 PCR-amplified and subsequently cloned into the entry vector pYr-1.1-GFP (YRBio, China) or
408 pYr-1.1-Halo to express GFP-tagged or Halo-tagged proteins, respectively. The LR
409 recombination reactions between the entry constructs and the destination vector
410 pAd/BLOCK-iT-DEST (YRBio, China) were carried out using LR Clonase II enzyme mix
411 (Thermo Fisher, 11791020), as described previously (Zhao et al., 2021).
412 To generate polyclonal antibodies of Kif9, the cDNA fragments encoding the indicated
413 amino acids (348-810 aa) were amplified by PCR and subcloned into pET-28a or pGEX-4T-1,
414 to express His-tagged or GST-tagged Kif9, respectively.
415 All constructs were validated by sequencing. The primers used for PCR amplification are
416 listed in Supplementary Table 1.

417 Mice

418 All animal experiments were performed following guidelines approved by the Institutional
419 Animal Care and Use Committee of Institute of Biochemistry and Cell Biology. The mice
420 used in this study had a genetic background of C57BL/6J. *Kif6*$^{+/-}$ and *Kif9*$^{+/-}$ mice were
421 obtained from GemPharmatech, China. Ages of mice used in this study were indicated in the
422 figures or the legends. gRNA sequences used for targeting *Kif6* or *Kif9* and primers used for
423 genotyping are listed in Supplementary Table 1.

424 Cell culture and transfection

425 HEK293T and HEK293A cells were grown in Dulbecco's modified Eagle's medium
426 (DMEM) (Thermo Fisher, 12430-054) supplemented with 10% fetal bovine serum (FBS)

427 (Ausbian, VS500T), 0.3 mg/ml glutamine (Sigma, G8540), 100 U/ml penicillin (Solarbio,
428 P8420) and 100 U/ml streptomycin (Solarbio, S8290). NIH3T3 cells were cultured in DMEM
429 medium with 10% normal goat serum (NGS), 0.3 mg/ml glutamine, 100 U/ml penicillin, and
430 100 U/ml streptomycin. hTERT-RPE1 and IMCD3 cells were cultured in DMEM/F12
431 medium (GE Healthcare) supplemented with 10% FBS, 0.3 mg/ml glutamine, 100 U/ml
432 penicillin, and 100 U/ml streptomycin. Additionally, RPE1 culture medium was supplemented
433 with 10 μg/ml hygromycin B (Thermo Fisher). All cell lines were passaged at a 1:4 ratio once
434 they reached 80%-90% confluency. HEK293A cells were used for packaging adenovirus
435 expressing GFP-tagged proteins following the guidelines (YRBio, China). All the cells were
436 routinely tested for mycoplasma contamination.

437 Primary culture of mouse ependymal cells (mEPCs) was prepared and cultured as
438 previously described (Delgehyr et al., 2015; Zhao et al., 2021). Newborn C57BL/6J mice
439 were anesthetized on ice, and the cerebellum, olfactory bulbs, meninges, and hippocampus
440 were carefully removed using sharp tweezers (Dumont, 1214Y84) in cold dissection solution
441 (5 mM Hepes, 161 mM NaCl, 5 mM KCl, 1 mM $MgSO_4$, 3.7 mM $CaCl_2$, and 5.5 mM
442 Glucose, pH 7.4) under a stereo microscope. The remaining telencephala were then digested
443 in a dissection solution containing 10 U/ml papain (Worthington-Biochem, LS003126),
444 0.2 mg/ml L-cysteine, 1.5 mM NaOH, 1 mM $CaCl_2$, 0.5 mM EDTA, and 0.15% DNase I
445 (Sigma-Aldrich, D5025) for 30 min at 37°C. After gentle pipetting and centrifugation at 1,500
446 rpm for 5 min at room temperature (r.t.), the cells were resuspended in DMEM medium
447 supplemented with 10% FBS and 1% penicillin/streptomycin and seeded into flasks (Sigma-
448 Aldrich, L2020) pre-coated with 10 μg/ml Human Plasma Fibronectin (Sigma-Aldrich,
449 FC010). Neurons were mechanically shaken off and removed by patting the flask
450 approximately 2 days after inoculation. When reaching ~90% confluence, cells were digested
451 with trypsin and re-plated into fibronectin-coated 29-mm glass-bottomed dishes (Cellvis,
452 D29-14-1.5-N) for immunofluorescence staining. Once cells were cultured to ~90%
453 confluency, FBS was removed from the medium to induce differentiation.

454 For the primary culture of mTECs, we followed the method described (Zhao et al.,
455 2021). mTECs were used to investigate the expression profile of *Kif6* and *Kif9* during the
456 differentiation of mTECs, because of their high induced differentiation efficiency.

457 For transfection of plasmids, cells were transfected at ~70% confluency with
458 Lipofectamine 2,000 (Thermo Fisher).

459 **Preparation and culture of whole-mounts of lateral ventricle walls**

460 Whole-mounts of the lateral ventricles were prepared as described (Ohata et al., 2014)
461 with minor modifications. Mice were euthanized with CO_2, and the lateral ventricles were
462 carefully dissected at a thickness of 500-1000 μm using Vannas Scissors (66VT, 54140B) in
463 pre-warmed (37°C) dissection solution (25 mM Hepes,117.2 mM NaCl, 5.3 mM KCl,
464 0.81 mM $MgSO_4$, 1.8 mM $CaCl_2$, 26.1 mM $NaHCO_3$, 1 mM $NaH_2PO_4 \cdot 2H_2O$, and 5.6 mM
465 Glucose, pH 7.4). The samples were subsequently cultured in DMEM supplemented with 0.3
466 mg/ml glutamine, 100 U/ml penicillin, and 100 U/ml streptomycin.

467 **Viral production and transfection**

468 Adenovirus particles were utilized to infect mEPCs or IMCD3 cells and produced in
469 HEK293A cells as previously described (Zhao et al., 2021). In brief, the adenovirus
470 expression constructs were linearized using *P*acI restriction enzyme (NEB) and transfected
471 into HEK293A cells cultured in 6-well plates using Lipofectamine 2,000 to produce the initial
472 adenovirus. When approximately 80% of the cells exhibited a cytopathic effect (CPE), the
473 culture medium was collected and infected HEK293A cells in a 10-cm dish. Once about 80%
474 of the cells showed a CPE, the culture medium was collected to infect fresh HEK293A cells
475 for viral amplification. When ~80% of the cells exhibited a CPE, both cells and the culture
476 medium were collected. To ensure complete release of the viral particles, three freeze-thaw
477 cycles (-80°C and 37°C) were performed, followed by centrifugation at 1,500 rpm for 5 min
478 to remove cell debris. The harvested adenoviral particles were used at a dilution of 1:1000 or
479 1:200.

480 **Immunofluorescence staining and imaging**

481 IMCD3 cells were fixed with 4% paraformaldehyde (PFA) in PBS, whereas mEPCs
482 grown on 29 mm glass-bottom dishes and freshly dissected whole-mounts were pre-
483 permeabilized with 0.5% Triton X-100 in PBS for 30 sec before fixation to remove soluble
484 proteins. After fixation, the cells were extracted with 0.5% Triton X-100 in PBS for 15 min
485 and blocked in 4% BSA in TBST at r.t. for 1 h. Next, the cells were incubated with primary
486 antibodies overnight at 4°C. After three washes with the blocking solution for 5 min each, the

487 cells were incubated with secondary antibodies at r.t. for 1h, and mounted in Dako (Dako,
488 S3023) or ProLong™ (Thermo Fisher, 2273640). All the antibodies used are listed in
489 Supplementary Table 2.

490 Fluorescent images were captured using a Leica TCS SP8 system with a HC PL APO
491 CS2 63 × /1.40 OIL objective or an Olympus Xplore SpinSR10 microscope with UPLAPO
492 OHR 60 ×/1.50 Objective Lens, and images were processed with maximum intensity
493 projections. 3D-SIM super-resolution images were taken with a DeltaVision OMX SR system
494 (GE Healthcare) and the z-axis scanning step was 0.125 μm. The original images were
495 processed for OMX SI Reconstruction, OMX Image Registration, and maximum intensity
496 projection with SoftWoRx software.

497 To perform GI-SIM imaging for mEPCs, the cells were seeded onto fibronectin-coated
498 12-mm coverslips and were infected with adenovirus one day prior to serum starvation. To
499 fluorescently label their multicilia, mEPCs were incubated with 100 nM SiR-tubulin
500 (Spirochrome, SC002) for 30 min or 200 nM Janelia Fluor® 549 HaloTag ligand (Promega,
501 GA1110) for 20 min. After labeling, mEPCs were gently laid flat against the bottom coverslip
502 and GI-SIM imaging was performed as described (Guo et al., 2018; Qiao et al., 2022). For
503 dual-color imaging, instrument calibration was conducted routinely with fluorescent beads.
504 The images and movies were processed using Fiji and Huygens softwares.

505 To record ciliary beating, the whole mounts of lateral ventricles were dissected and cut at
506 a thickness of 500-1000 μm as previously described (Ohata et al., 2014; Zhao et al., 2021). To
507 label the cilia, 100 nM SiR-tubulin was added to the culture medium and incubated for 1 h.
508 High-speed live imaging was conducted at 37℃ using an Olympus Xplore SpinSR 10
509 microscope equipped with UPLAPO OHR 60 × /1.50 Objective Lens, Hamamatsu ORCA-
510 Fusion camera, 4,000 rpm CSU Disk Speed, and OBIS Laser. Ciliary beat was captured at
511 100 frames per second (fps) by a time-lapse collection of single optical sections with 80%
512 laser power (640 nm) to achieve an exposure time of 5 ms. Kymographs were generated for
513 the first 500 ms using Fiji.

514 The ependymal flow assay was performed as described (Liu et al., 2021; Mirzadeh et al.,
515 2010) with minor modifications. Briefly, the freshly dissected ependyma was sliced using a

vibratome (Leica VT1000S) to obtain slices with a thickness of 250 μm. Before imaging, multicilia were labeled with 100 nM SiR-tubulin for 1 h and small fluorescent latex beads with a diameter of 250 nm at 1:500 dilution (Invitrogen, F8809) were added to the culture medium. Time-lapse microscopy was performed at 37 ℃ using using an Olympus Xplore SpinSR10 microscope equipped with UPLAPO OHR 60 × /1.50 Objective Lens. The laser power for the beads channel (561 nm) was adjusted based on the fluorescent intensity, and exposure time was set to 100 ms. The laser power for the SiR-tubulin channel (640 nm) was set to 80% to achieve an exposure time of 5 ms.

During recording, fluorescent beads suspended in the culture medium containing the living ependymal tissues were imaged at a fixed z-plane to record their motility. Subsequently, multicilia in the same areas were visualized by adjusting the focal plane, and live imaging of a single optical section was conducted to record ciliary motility. All frames of beads in the same area were projected together from Movies 11-12 and superimposed with trajectories of traceable, rapidly-moving bead aggregates in the first 500 ms to show flow directions and tracks. The velocity of beads was meausured using Fiji.

To record sperm motility, sperm were released from cauda epididymidis into buffer (Njabsw, M1130), and followed by live imaging with a spinning disk confocal microscope at a fixed z-plane and at 25-ms intervals. Two pair of P88 wild-type mice and *Kif6*$^{-/-}$ litermates were performed.

Immunoblotting

Immunoblotting experiments were performed as described (Zhao et al., 2021). To prepare tissue lysates, freshly dissected tissues from mice were placed in ice-cold RIPA buffer (50 mM Tris-HCl, 150 mM NaCl, 1% NP-40, 0.5% Sodium Deoxycholate, 0.1% SDS, and 1 mM EDTA, pH7.5) supplemented with protein inhibitors cocktail. The tissues were homogenized using the homogenizer Precellys 24 system (Bertin, France). The lysates were cleared by centrifugation at 13,200 rpm at 4°C for 15 min, and mixed with an equal volume of 2 × SDS-PAGE loading buffer (100 mM Tris-HCl, 4% SDS, 20% glycerol, 2% 2-mercaptoethanol, 0.1% bromophenol blue, pH 6.8). For cultured cells, cells were washed with pre-warmed PBS and lysed in 2 × SDS-PAGE loading buffer. The lysates were boiled at 100°C for 10 min and then subjected to immunoblotting.

546

547 **Electron microscopy**

548 For scanning electron microscopy (SEM), mice were deeply anesthetized with 360
549 mg/kg body weight of avertin (Sigma-Aldrich, T48402) by intraperitoneal injections. The
550 tissues were dissected after transcardial perfusion with 4% PFA in PBS using an injection
551 pump (Smiths medical, WZS-50F6, 250 ml/h). The dissected tissues were post-fixed with
552 2.5% glutaraldehyde at 4°C overnight. Subsequently, the tissues were treated with 1% OsO_4
553 at 4°C for 1 h and dehydrated with a graded series of ethanol. Critical point drying (Leica EM
554 CPD300) was performed before metal shadowing (40 mA, 60 s). Images were captured using
555 a FEI Quanta 250 scanning electron microscope.

556 For transmission electron microscoy (TEM), the tissues were fixed in 2.5%
557 glutaraldehyde/PBS at 4°C overnight, washed with PBS, and treated with 1% OsO_4 for 1.5 h
558 at r.t.. The tissues were dehydrated with a graded series of ethanol and further dehydrated with
559 acetone. Subsequently, the samples were embedded in Epon 812 resin at 60°C for 48 h. Thin
560 sections of 70 nm thickness were obtained using an ultramicrotome (Leica EM PACT2) and
561 stained with 2% uranyl acetate for 15 min, followed by 1% lead citrate for 5 min. The images
562 were captured using a FEI Tecnai G2 Spirit Twin transmission electron microscope and
563 analyzed using Fiji software.

564 **Coronal brain section**

565 Coronal brain slices with a thickness of 250 μm were achieved using a vibratome
566 sectioning technique, as previously described (Chen et al., 2020). Mice were deeply
567 anesthetized with 360 mg/kg body weight of avertin administered via intraperitoneal
568 injections. Transcardial perfusion was performed using PBS followed by 4% PFA in PBS,
569 utilizing an injection pump (Smiths medical, WZS-50F6, 250 ml/h). Whole brains were
570 dissected from the mice and cut using a vibratome to obtain coronal slices with a thickness of
571 250 μm. These slices were placed into 35-mm glass-bottom dishes (Cellvis, D35-20-1.5-N)
572 and were imaged with an Olympus SZX16 Stereo Microscope.

573 **Reproductive performance test**

574 Mating test was perform as previously described (Miyata et al., 2020). 2-3 month-old
575 *Kif6*$^{-/-}$ and *Kif9*$^{-/-}$ male mice with normal appearance were individually caged with two age-

appropriate heterozygous female mice for four months and two *Kif6*$^{-/-}$ and *Kif9*$^{-/-}$ female mice were separately caged with one heterozygous male mice, and then were checked regularly every several days. The number of pups was counted during the period. Two independent experiments were carried out.

Phylogenomic analysis and multiple alignment

The phylogenetic tree and taxonomic groups were constructed based on literatures and Taxonomy Browser of National Center for Biotechnology Information (NCBI) (Cetkovic et al., 2018; Mukherjee and Brocchieri, 2013). The protein database of NCBI were searched to identify genes with orthologous proteins of Kif6 and Kif9 across a wide range of species (such as mammals, birds, amphibians, fishes, jawless vertebrates, cephalochordates, urochordates, echinoderms, nematodes, mollusks, flatworms, cnidarians, placozoans and protozoans) using the full-length murine protein sequences of Kif6 and Kif9 as queries.

The selected sequences were aligned using COBALT searches with default settings. Genebank accession numbers of Kif6 and Kif9 orthologues were provided in Supplemenatry Figure 1a. Only alignment columns without gaps were colored, with highly conserved positions shown in red and less conserved positions shown in blue.

Analysis of BB rotational polarity

BB rotational polarity was analyzed as previously described (Guirao et al., 2010; Mirzadeh et al., 2010; Ryu et al., 2021). In TEM images, the BB rotational polarity was determined by drawing a unit vector from the center of a BB to the vertex of its BF. The mean vector length within a given field in each full-size electron micrograph (2,048 pixels × 2,048 pixels) was calculated using Microsoft Excel software (Microsoft). In 3D-SIM images, the BB rotational polarity was determined by drawing a unit vector from the geographic center of Cep164 ring (BB distal end marker) to the center of either Centriolin or γ–tubulin signals (BF marker). The mean vector length within a cell was calculated using Excel software (Microsoft) to demostrate the extent of the rotational polarity.

Quantification and statistical analysis

BB numbers were assessed without knowledge of the genotypes and were measured from 3D-SIM images using Cep164-positive ring as a BB marker. The BB center and cell

605 border center were determined using the default setting of the "ROI Manager" function in
606 Fiji.
607 All experiments, unless otherwise stated, were independently repeated at least twice for
608 both microscopic or biochemical results. Statistical results are presented as mean ± SD.
609 Unpaired two-tailed student's *t*-test was performed using GraphPad Prism 9.0 software, and
610 differences were considered significant at $P < 0.05$. Data analyses were performed in a
611 blinded manner, with the researchers performing the quantification being unaware of the
612 genotype.

613 **Acknowledgements.**
614 The authors thank Profs. Lan Bao and Dr. Lei Diao (Center for Excellence in Molecular
615 Cell Science, CAS) for the reagents and technical assistance, Profs. Xin Liang (Tsinghua
616 University) and Profs. Wei Feng (Institute of Biophysics, CAS) for technical help and
617 valuable discussions, and the staff members of the Integrated Laser Microscopy System at the
618 National Facility for Protein Science in Shanghai (NFPS) (Shanghai Advanced Research
619 Institute, CAS) and core facilities of the Center for Excellence in Molecular Cell Science
620 (CEMCS) for instrumental and technical supports. This work was supported by National
621 Natural Science Foundation of China (31991192, 32230027 and 32270725).

622 **Declaration of interests**
623 The authors declare no competing financial interests.

624 **Author contributions**
625 X.Y. and X.Z. conceived and supervised the project; C.F., X.P. and Di Li performed the
626 research; Dong Li contributed to GI-SIM imaging; Y.C., L.L. and Q.G. assisted with
627 experiments; X.Y., X.Z., C.F. and X.P. collectively analyzed data and wrote the manuscript,
628 with input from all authors.

629 **Figure legends**

630 **Figure 1. Molecular characterization and subcellular localization of mammalian *Kif6***
631 **and *Kif9*. (a)** Schematics of full-length murine Kif6 and Kif9. The motor and coiled-coil
632 domains were identified using Conserved Domain Search Service of NCBI and SMART
633 (Simple Modular Architecture Research Tool) (http://smart.embl.de). **(b)** Conservation of *Kif6*

and *Kif9* across species with motile cilia and/or flagella throughout the evolution process. The phylogenetic tree and taxonomic groups were referrenced from literature (Cetkovic et al., 2018; Mukherjee and Brocchieri, 2013). **(c)** mRNA expression profile of *Kif6* and *Kif9* during multiciliation. The gene expression profiles were obtained from our previous cDNA microarray analysis of mTECs cultured at an air-liquid interface (ALI) for the indicated days (Xu et al., 2015). Expression patterns of genes crucial for cilia formation (*Ift88* and *Ift122*) and BB amplification (*Cep152*), were listed for comparison. **(d)** Expression patterns of Kif6 and Kif9 during multiciliation of mTECs. Multicilia formation is indicated by increased levels of Ift81, Bbs3 and acetylated tubulin (Ac-tub). Gapdh served as loading control. **(e, f)** Abundance of Kif6 and Kif9 in mouse tissues (**e**) and cultured cells (**f**) containing motile cilia. Tissues from a 2-month-old male mouse were dissected and lysed. mEPCs were harvested on day 8 post serum starvation. RPE1, NIH3T3 and IMCD3 cells were serum-starved for 48 h to induce ciliogenesis. Gapdh or β-actin served as loading control. **(g)** Experimental scheme for (**h, j-l and Supplementrary Fig. 2**). Precursors of mEPCs were isolated from P0 mouse brain and serum-starved on day 0 to induce to differentiate into multiciliated cells. Cells were fixed on day 8 for immunofluorescence (IF) staining and imaged by confocal microscopy or 3D-SIM. To express GFP-tagged proteins, cells were infected with adenovirus on day-1. **(h)** Endogenous Kif6 and Kif9 localized in multicilia. Ac-tub labeled ciliary axonemes (arrowheads). **(i)** Kif6 and Kif9 did not localize in primary cilia. IMCD3 cells were harvested at day 2 post serum starvation, and fixed for immunostaining, followed by confocal microscopy. DAPI marked nucleus. Cilia pointed by arrowheads were zoomed in 2× to show details. **(j)** Exogenous Kif6-GFP and Kif9-GFP localized at the axonemes of multicilia. **(k, l)** Typical 3D-SIM images of endogenous Kif9 and Kif6. Kif9 was enriched in the central lumen (**k**), while Kif6 localized as punta along peripheral DMTs (**l**). Ac-tub and Hydin served as axoneme and CP markers, respectively. Cilia pointed were magnified by 200% for details. Corresponding line scans at the indicated region of the magnified insets showed colocalization of Kif9 with Hydin (**k**), and Kif6 distributed along the axoneme with Ac-tub (**l**). Illustrations are provided to aid comprehensions.

Figure 2. Kif6, differed from Kif9, moves along axonemal MTs and colocalizes with IFT particles. Quantification results are presented as mean ± SD and subjected to unpaired two-tailed student's *t*-test: $*P < 0.05$. **(a)** Experimental scheme for ciliary trafficking recorded by GI-SIM. mEPCs were infected with adenovirus at day-1 and imaged during day 5-8. **(b)** Expression levels of GFP-tagged proteins in day 7 mEPCs. Immunoblotting was performed using GFP, Kif6, Kif9 and Ift81 antibodies, respectively. A star indicates a non-specific band closed to Ift81-GFP. **(c-e)** Ciliary movement of Ift81-GFP (**c**), Kif6-GFP (**d**) and Kif9-GFP (**e**). Both Ift81-GFP (**c**) and Kif6-GFP (**d**) were able to move along the axonemal outer DMTs while the motility of Kif9-GFP (**e**) was not detectable. Images were recorded at 25 frames per sec (fps). The trafficking trajectories of GFP-tagged puncta through a time projection of the first 200 frames from Movies 1-3 were showed. Typical cilia framed were magnified by 300% to show detailed bidirectional transports of GFP-fusion puncta. The clear and traceable GFP-tagged particles were marked and corresponding kymographs were presented. In (**c**), two GFP-tagged particles (labeled by 1, 3) and two (labeled by 2, 4) were showed for anterograde and retrograde transports, respectively. In (**d**), two GFP-tagged particles (labeled by 1, 2) and one (labeled by 3) were showed for anterograde and retrograde transports, respectively. (**f, g**) Quantification results of velocities and frequencies from the indicated numbers of particles (**f**) and cilia (**g**). Antero: Anterograde transport; Retro: Retrograde transport. **(h, i)** Colocalization of Kif6-GFP and IFT protein (Ift56) at axonemes by confocal (**h**) and 3D-SIM (**i**). Ac-tub marked ciliary axoneme. A typical cilium was magnified by 400% to show details. Line scans at the indicated regions (I and II) exihibited the colocalization of Kif6-GFP and Ift56 along the axoneme. Co-localized punta were pointed by yellow arrowheads.

Figure 3. Kif6-GFP punta move together with IFT particles along the axoneme. (a-c) Ciliary trafficking of fluorescent particles. mEPCs were infected with adenovirus expressing of Kif6-GFP and Ift27-Halo and dual-color time-lapse live imaging was taken at 14 fps. Three distinct bidirectional moving particles within cilia were observed: particles labeled with both Ift27-Halo and Kif6-GFP ($Ift27^{+}Kif6^{+}$ particles) (**a**, **b**), those labeled only with Kif6-GFP

(Kif6^{+} particles), and those labeled only with Ift27-Halo (Ift27^{+} particles). Ciliary trafficking trajectories of GFP/Halo-tagged puncta were projected by the first 200 frames from Movies 4-5. Typical cilia pointed were magnified by 300% to display traceable anterograde and retrograde transports of Ift27^{+}Kif6^{+} particles (**a, b**), Kif6^{+} particles (**c**) and Ift27^{+} particles (**c**) from representative frames, respectively. The clear and traceable particles are indicated by colored arrows or arrowheads in magnified cilia. Corresponding kymographs were presented. **(d, e)** Quantification and velocities of three types particles of anterograde and retrograde transports. 45 clear cilia from 4 cells co-expressed Kif6-GFP with Ift27-Halo were scored. The corresponding particles number (n) was presented.

Figure 4. Knockout of *Kif6* or *Kif9* leads to hydrocephalus and male infertility. (a) Schematic for generating *Kif6* (top) and *Kif9* (bottom) knockout mice using CRISPR/Cas9 technique. The targeting of sgRNA (scissors) and genotyping PCR primers were indicated for each knockout model. **(b)** Representative genotyping PCR results. Genomic DNAs were extracted from P21 mice tails and amplified by PCR using the indicated primers in (**a**). **(c)** Complete depletion of Kif6 and Kif9 proteins in the indicated tissues. Tissue lysates were prepared from 2-month-old mice of the indicated genotypes. Gapdh served as a loading control. **(d, e)** Morphologies of *Kif6* and Kif9 deficient mice. *Kif6*$^{-/-}$ mice exhibited a dome-shaped skull (arrow) and kyphosis (arrowhead) with skinny bodies (**d**). In contrast, *Kif9*$^{-/-}$ mice showed a normal appearance (**e**). **(f, g)** Representative images of coronal brain sections of *Kif6*$^{-/-}$ (**f**) or *Kif9*$^{-/-}$ (**g**) and their corresponding wide-type littermates. M: month. **(h)** Quantification of mice with enlarged ventricles (n = 60 for *Kif6*$^{-/-}$; n = 11 for *Kif9*$^{-/-}$ mice). **(i)** Survival curves of mice in indicated genotypes during a 12-month observation period. Numbers of mice used for each genotype were indicated. **(j, k)** Morphology and motility of sperm from wide-type and *Kif6*$^{-/-}$ littermates. Sperm motility trajectories were color-coded through projection of the first 50 frames (**k**). Two pairs of P88 *Kif6*$^{-/-}$ mice and wild-type liitermates were used. Refer to Movie 7.

Figure 5. Knockout of *Kif6* impairs planar polarity of cilia across the ependyma.

Quantification results are pooled together (mean ± SD plus sample dots) and subjected to unpaired two-tailed student's *t*-test: $*P < 0.05$. M: mild hydrocephalus mice with normal appearance but larged ventricles; S: severe hydrocephalus mice with the observable dome-shaped skull like Fig. 1d. **(a)** Schematic of experimental design. Whole-mounts of ventricle walls were freshly dissected and subjected to electron microscopy (EM) or live cell imaging. SiR-tubulin, a fluorescent dye for MTs, was used to label cilia. Ciliary motility was live-cell imaged at a single optical section with 10-ms intervals. An illustration of the beat pattern of an ependymal cilium, depicted as a side view, is provided for better comprehension. **(b)** Representative SEM images of ependymal multicilia from wild-type and *Kif6*$^{-/-}$ littermates at P4 (top) and P30 (bottom). **(c)** Representative side-view cilia beat images. Cilia beat patterns in individual cells were unaffected by *Kif6*-deficiency. Two consecutive cycles of cilia beat patterns were showed. The beat direction was indicated by color-coded arrows, followed by pseudo-coloring and merging. Representative top-view images from another pair of littermates were presented in Supplementary Fig. 4b. **(d)** Quantification of ciliary beating frequencies. Results were from 5 pairs of littermates with 60 cells per mouse. (**e**) Unidirectional multicilia beat across ependyma was disrupted by the loss of Kif6. The first three consecutive frames cropped from Movies 8-9, were pseudo-colored and overlaid to show ciliary motilities. Beating directions of multicilia are indicated by arrows. Representative images of another two pairs of littermates were presented in Supplementary Fig. 4c. **(f)** Representative top-view images of cilia beat patterns in *Kif9*-deficient mice. Two consecutive cycles of cilia beat patterns are presented. Representative side-view fields from another pair of littermates were presented in Supplementary Fig. 4d. **(g)** Tissue-wide polarity of cilia beating was not altered in *Kif9*-deficient ependyma. The first three consecutive frames cropped from Movies 9-10, were pseudo-colored and merged to show ciliary motilities. Additional representative images were presented in Supplementary Fig. 4e. **(h)** Representative projections of bead movements from Movies 12-13. Trajectories of traceable, rapidly-moving beads in the first 500 ms were superimposed to show flow directions. **(i)** Quantification of bead velocities. Results from two pairs of P36 and one pair of P48 littermates, with 60 traceable beads for each.

Figure 6. *Kif6* deficiency impairs rotational polarity of BBs in ependymal tissues.

Quantification results are pooled together (mean ± SD plus sample dots) and subjected to unpaired two-tailed student's *t*-test: $*P < 0.05$. **(a)** Structural features of a motile cilium. Top and bottom panels illustrate the side view of the cilium and typical transverse view of the BB, respectively. BB polarity marked by its conical BF that extends laterally to the MT triplet. **(b-f)** The loss of Kif6, but not Kif9, impaired rotational polarity. Ependymal tissues from the indicated mice were immunostained for Cep164 to visualize BBs and γ-tubulin to visualize BFs. Framed regions (**c, e**) were magnified to show the rotational polarity of BBs in individual cells **(b, c)**. The BF orientations are indicated by arrows (**b, d**). Note the misorangized rotational polarity in both cellular and tissue-level in *Kif6*$^{-/-}$ ependyma. Mean vector lengths (**f**) were scored from 20 cells each mouse. Mice used were two 6-month-old (6M) and one 7-month-old (7M) mice for *Kif9*$^{-/-}$ and three of their wild-type littermates; two P34, one P43 mice with severe hydrocephalus (Se) and one P62 mouse with mild hydrocephalus (Mi) for *Kif6*$^{-/-}$ and their corresponding wild-type littermates. **(g, h)** Representative TEM images (**g**) and quantification analysis on the extent of rotational polarity (**h**). BF orientations are indicated by arrows. The mean vector length (**h**) was calculated from BBs with clear BFs in at least ten full-size electron micrographs and over 130 BFs were scored for each genotype. **(i)** Illustrations are provided to aid comprehensions on the functions of Kif9 (top) and Kif6 (bottom) in the rotational polarity of BBs. **(j)** The number of BBs in ependymal cells was not altered by *Kif6* or *Kif9*-deficiency. 50 cells were measured per mouse. **(k)**. A summarizing model showing the distinct functions of *Kif6* and *Kif9* in motile cilia. Kif6 may be involved in material transport associated with a specific IFT machinery, or transport cargo on its own, thus thereby ensuring BB polarity and the coordinated ciliary beat. Kif9 may regulate ciliary beat by inducing changes on subtle structure related to conformation. BB, basal body; BF, basal foot; CP, central pair; DMT, doublet microtubule; TF, transition fiber; TZ, transition zone.

Legends for Supplementary Figures

Supplementary Figure 1. Comparison of murine Kif6 and of Kif9 (related to Fig. 1). (a) Sequence alignment of Kif6 (left) and Kif9 (right) orthologues as indicated Fig. 1b. Highly conserved positions were shown in red and less conserved positions shown in blue. The

sequences of Kif6 orthologues used were: mouse (NP_796026.2), human (NP_659464.3), chicken (XP_003640993.5), frog (NP_001106482.1), zebrafish (NP_001070899.1), lancelet (XP_035685117.1), ascidian (XP_002124970.1), sea urchin (XP_030854411.1), mussel (CAG2221785.1), flatworm (PAA61917.1), sea anemone (XP_032228212.2), *Trichoplax* (RDD42533.1), *Tetrahymena* (XP_001024804.2), *Trypanosoma* (XP_846346.1) and green algae (XP_042928646.1). The sequences of Kif9 orthologues used were: mouse (NP_001157041.1), human (NP_001400904.1), chicken (XP_040522129.1), frog (XP_012821147.1), zebrafish (XP_001922460.1), lancelet (XP_035663761.1), ascidian (XP_018668035.1), sea urchin (XP_030830023.1), mussel (CAG2242108.1), flatworm (PAA61899.1), sea anemone (XP_001636554.1), *Trichoplax* (RDD45058.1), *Tetrahymena* (XP_001022313.1), *Trypanosoma* (RHW71316.1) and green algae (P46870.1). Multiple sequence alignments were obtained using COBALT (NCBI). **(b)** Protein sequence alignment of motor domains (Kif6-MD, 1-353 aa; Kif9-MD, 1-348 aa). The alignment was generated by the COBALT sequence alignment program using default parameters. Genebank accession numbers of proteins were as follows: Kif6 (NP_796026.2) and Kif9 (NP_001157041.1). The motors were identified using SMART.

Supplementary Figure 2. The localization of exogenous Kif6 and Kif9 within motile cilia (related to Fig. 1). mEPCs were harvested at day 8 and fixed for immunostaining, followed by 3D-SIM. **(a, b)** Localization of Kif6-GFP (**a**) and Kif9-GFP (**b**) in the axonemes of multicilia. Kif6-GFP exhibited punctate localization along the axonemal DMTs whereas Kif9-GFP was enriched in CP lumen. Spef1 served as the CP marker. Typical cilia were magnified by 200% to highlight details. Line scans were generated at the indicated positions by white lines in merged images.

Supplementary Figure 3. Kif6 moves along the axoneme and colocalizes with IFT particles (related to Fig. 2 and 3). (a) Kif6-GFP, but not Kif9-GFP, resembling Ift81-GFP, moved along the axonemal DMTs. The trafficking trajectories of GFP-tagged puncta were visualized through projection of the first 200 frames. Typical cilia were magnified by 300% to show the detailed anterograde transport of GFP-fusion puncta. The clear and traceable GFP-tagged particles were marked and corresponding kymographs were presented. **(b, c)** Kif6-

GFP co-localized with IFT protein (Ift88) at axonemes from confocal (**b**) and 3D-SIM images (**c**). Ac-tub marked ciliary axoneme. A typical cilium was zoomed in 4× for details. Line scan at the indicated region exihibited the colocalization of Kif6-GFP and Ift88 along the axoneme (**c**). (**d**) Calibration of the microscope. Instrument calibration was conducted routinely with fluorescent beads before dual-color GI-SIM imaging experiments. A line scan was performed along the white line to determine the alignment.

Supplementary Figure 4. *Kif6* deficiency disrupts PCP of cilia beat across ependyma (related to Fig. 6). Quantification results are pooled together (mean ± SD plus sample dots) and subjected to unpaired two-tailed student's *t*-test. **(a)** Representative TEM images of ependymal cilia from wild-type and *Kif6*$^{-/-}$ mice. CP MTs (arrow); inner and outer dynein arms (arrowheads); transition zone (TZ, indicated by yellow lines); basal body (BB, indicated by yellow lines) (n =2 biological replicates). **(b)** Representative top-view images of Cilia beat pattern from *Kif6*$^{-/-}$ mice and wild-type littermates. At least two beat cycles from consecutive images were exhibited. The beat directions of the initial cycle are indicated by arrows, followed by pseudo-coloring and merging. **(c)** Cilia beat directions across ependyma by *Kif6*-deficency. The first three consecutive frames were pseudo-colored and overlaid to show ciliary beat directions. **(d)** Representative side-view cilia beat images. At least two consecutive cycles of cilia beat were presented. The beat direction is indicated by color-coded arrows, followed by pseudo-coloring and merging. **(e)** Cilia beat directions across ependyma by *Kif9*-deficency. Beat directions of multicilia (white arrows) in representative microscopic fields were presented. **(f)** Ciliary beat frequencies of *Kif9*$^{-/-}$ ependymal cilia. Quantification results were from 3 pairs of littermates with 50 cells per mouse. S: Severe hydrocephalus mice with obvious dome-shaped skull. M: mild hydrocephalus mice with normal morphological appearance but enlarged ventricles.

Supplemental Figure 5. *Kif6* deficiency disrupts the rotational polarity of BBs in ependyma (related to Fig. 7). (a-d) BBs in *Kif6*$^{-/-}$ **(c, d)** but not in *Kif9*$^{-/-}$ (**a, b**) ependymal cells displayed impaired rotational polarity. Ependymal tissues from the indicated littermates were co-immunostained for Cep164 to visualize BBs and Centriolin to visualize BFs. Framed regions in (**b, d**) were maginified to show BF orientations (arrows) in (**a, c**). Arrows in (**b**, **d**)

indicate rotational polarities of the wild-type, *Kif9*$^{-/-}$ and *Kif6*$^{-/-}$ BB patches, which broadly point to one direction in the microscopic field. **(e)** Quantification of the rotational polarity. Results from three mice per genotype were presented as mean ± SD plus sample dots and subjected to unpaired two-tailed student's *t*-test: $*P < 0.05$. Mice used were: two 6-month-old (6M) and one 7-month-old (7M) mice for *Kif9*$^{-/-}$ and three of their wild-type littermates; three P35 mice with severe (S) hydrocephalus for *Kif6*$^{-/-}$ and three of their wild-type littermates. 50 ependymal cells were scored for each mouse.

Supplementary Figure 6. The translational polarity was not affected by *Kif6* deficiency (related to Fig. 7). Pooled results from three mice per genotype were presented as mean ± SD plus sample dots and subjected to unpaired two-tailed student's *t*-test: $*P < 0.05$. **(a-d)** *Kif6* deficiency did not impair the transitional polarity of BBs. Ependymal tissues from two P62 and one P68 *Kif6*$^{-/-}$ mice of mild (M) hydrocephalus, three severe (S) hydrocephalus (P34, P38 and P43) and six of their wild-type littermates were immunostained for ZO1 and Cep164 to visualize cell borders and BBs, respectively (**a**). BB patch displacement relative to the cellular geographic center (**c**) and relative BB patch area (**d**) were quantified as illustrated in (**b**). 50 ependyma cells were scored for each mouse.

Legends for supplementary movies

Movie 1. Bidirectional motility of ciliary Ift81-GFP puncta (related to Fig. 2c). mEPCs were infected with adenovirus at day-1 and imaged during day 5-8 by GI-SIM. Images were recorded at 25 frames per sec (fps) and the playback speed is 20 fps. Typical cilia framed were magnified by 300% to show detailed bidirectional transports of Ift81-GFP puncta.Two particles (labeled by 1, 3) and two (labeled by 2, 4) were showed for anterograde and retrograde transports, respectively.

Movie 2. Bidirectional motility of ciliary Kif6-GFP puncta (related to Fig. 2d). mEPCs were treated, imaged, and presented as described in Movie 1. Typical cilia framed were magnified by 300% to show detailed bidirectional transports of Kif6-GFP puncta. Two particles (labeled by 1, 2) and one (labeled by 3) were showed for anterograde and retrograde transports, respectively.

Movie 3. Kif9-GFP does not exhibit progressive movement along the cilia (related to Fig. 2e). mEPCs were treated, imaged, and presented as described in Movie 1. Typical cilia framed were magnified by 300% to show details.

Movie 4. Ciliary Kif6-GFP punta move together with IFT particles (related to Fig. 3a, b). mEPCs were infected with adenovirus expressing Kif6-GFP and Ift27-Halo, and dual-color time-lapse live imaging was taken by GI-SIM. Images were recorded at 14 fps and the playback speed is 20 fps. Typical cilia pointed were magnified by 300% to display traceable anterograde (Fig. 3a) and retrograde (Fig. 3b) transports of $Ift27^{+}Kif6^{+}$ particles from representative frames, respectively. Two particles (labeled by 1, 2) and one (labeled by 3) were showed for anterograde and retrograde transports, respectively.

Movie 5. Ciliary Kif6-GFP punta and IFT particles move separately (related to Fig. 3c). mEPCs were treated, imaged, and presented as described in Movie 4. Typical cilia pointed were magnified by 300% to display traceable anterograde and retrograde transports of $Kif6^{+}$ particles or $Ift27^{+}$ particles (related to Fig. 3c) from representative frames, respectively. Two particles (labeled by 5, 6) and two (labeled by 4, 7) were showed for anterograde and retrograde transports, respectively.

Movie 6. A representative sperm motility from *Kif9*$^{+/+}$ and *Kif9*$^{-/-}$ male mice. Sperm were released from cauda epididymidis, followed by live imaging with a spinning disk confocal microscope at a fixed z-plane and at 25-ms intervals. The playback speed is 20 fps. One pair of P80 wild-type (top) mice and *Kif9*$^{-/-}$ (bottom) litermates were presented.

Movie 7. A representative sperm motility from *Kif6*$^{+/+}$ and *Kif6*$^{-/-}$ male mice (related to Fig. 5k). Sperm were released, imaged, and presented as described in Movie 6. One pair of P88 wild-type (top) mice and *Kif6*$^{-/-}$ (bottom) litermates were presented.

Movie 8. Representative ciliary beat patterns in *Kif6*$^{+/+}$ ependyma (related to Fig. 6e). P31 WT ependyma was freshly dissected and labeled with SiR-tubulin, followed by live imaging with a spinning disk confocal microscope at a fixed z-plane and at 10-ms intervals. The playback speed is 5 fps. Images of the first three frames are presented in Figure 6e.

Movie 9. Representative ciliary beat patterns in *Kif6*$^{-/-}$ ependyma (related to Fig. 6e). P31 *Kif6*$^{-/-}$ ependyma was treated, imaged, and presented as described in Movie 8. The mouse used was a littermate of the one in Movie 9, and exhibited severe hydrocephalus. Images of the first three frames are presented in Figure 6e.

Movie 10. Representative ciliary beat patterns in *Kif9*$^{+/+}$ ependyma (related to Fig. 6g). 7M WT ependyma was treated, imaged, and presented as described in Movie 9. Images of the first three frames are presented in Figure 6g.

Movie 11. Representative ciliary beat patterns in *Kif9*$^{-/-}$ ependyma (related to Fig. 6g). 7M *Kif9*$^{-/-}$ ependyma was treated, imaged, and presented as described in Movie 8. The mouse was a littermate of the one in Movie 10. Images of the first three frames are presented in Figure 6g.

Movie 12. Representative liquid flows driven by ciliary beat in *Kif6*$^{+/+}$ ependyma (related to Fig. 6h). Fresh ependyma from a P36 wild-type mouse were incubated with SiR-tubulin to label cilia and fluorescent latex beads as flow indicators. Beads motilities were imaged with a spinning disk confocal microscope at 100-ms intervals and at a fixed z-plane. The playback speed is 5 fps. Trajectories of 8 traceable, rapidly-moving aggregated beads in the first 500 ms were shown.

Movie 13. Representative liquid flows driven by ciliary beat in *Kif6*$^{-/-}$ ependyma (related to Fig. 6h). Fresh ependymal tissues from a P36 *Kif6*$^{-/-}$ mouse with severe hydrocephalus were treated, imaged, and presented as described in Movie 12. Trajectories of 13 traceable, rapidly-moving aggregated beads in the first 500 ms were shown.

Legends for Supplementary Tables

Supplementary Table 1 Sequences of primers and gRNAs.

Supplementary Table 2 List of antibodies.

References

1. Bernstein, M., Beech, P.L., Katz, S.G., and Rosenbaum, J., L. (1994). A New Kinesin-like Protein (Kip1) Localized to a Single Microtubule of the Chlamydomonas Flagellum. J Cell Biol *125*, 1313-1326.

2. Bhogaraju, S., Cajanek, L., Fort, C., Blisnick, T., Weber, K., Taschner, M., Mizuno, N., Lamla, S., Bastin, P., Nigg, E.A., *et al.* (2013). Molecular basis of tubulin transport within the cilium by IFT74 and IFT81. Science *341*, 1009-1012.
3. Boutin, C., Labedan, P., Dimidschstein, J., Richard, F., Cremer, H., Andre, P., Yang, Y., Montcouquiol, M., Goffinet, A.M., and Tissir, F. (2014). A dual role for planar cell polarity genes in ciliated cells. Proc Natl Acad Sci U S A *111*, E3129-3138.
4. Buchan, J.G., Gray, R.S., Gansner, J.M., Alvarado, D.M., Burgert, L., Gitlin, J.D., Gurnett, C.A., and Goldsmith, M.I. (2014). Kinesin Family Member 6 (kif6) Is Necessary for Spine Development in Zebrafish.
5. Bustamante-Marin, X.M., Yin, W.N., Sears, P.R., Werner, M.E., Brotslaw, E.J., Mitchell, B.J., Jania, C.M., Zeman, K.L., Rogers, T.D., Herring, L.E., *et al.* (2019). Lack of GAS2L2 Causes PCD by Impairing Cilia Orientation and Mucociliary Clearance. Am J Hum Genet *104*, 229-245.
6. Butler, M.T., and Wallingford, J.B. (2017). Planar cell polarity in development and disease. Nat Rev Mol Cell Biol *18*, 375-388.
7. Cason, S.E., and Holzbaur, E.L.F. (2022). Selective motor activation in organelle transport along axons. Nat Rev Mol Cell Biol *23*, 699-714.
8. Cetkovic, H., Harcet, M., Roller, M., and Bosnar, M.H. (2018). A survey of metastasis suppressors in Metazoa. Lab Invest *98*, 554-570.
9. Chen, Y., Zheng, J., Li, X., Zhu, L., Shao, Z., Yan, X., and Zhu, X. (2020). Wdr47 Controls Neuronal Polarization through the Camsap Family Microtubule Minus-End-Binding Proteins. Cell Rep *31*, 107526.
10. Chien, A., Shih, S.M., Bower, R., Tritschler, D., Porter, M.E., and Yildiz, A. (2017). Dynamics of the IFT machinery at the ciliary tip. eLife *6*.
11. Clare, D.K., Magescas, J., Piolot, T., Dumoux, M., Vesque, C., Pichard, E., Dang, T., Duvauchelle, B., Poirier, F., and Delacour, D. (2014). Basal foot MTOC organizes pillar MTs required for coordination of beating cilia. Nat Commun *5*.
12. Delgehyr, N., Meunier, A., Faucourt, M., Bosch Grau, M., Strehl, L., Janke, C., and Spassky, N. (2015). Ependymal cell differentiation, from monociliated to multiciliated cells. Methods Cell Biol *127*, 19-35.
13. Demonchy, R., Blisnick, T., Deprez, C., Toutirais, G., Loussert, C., Marande, W., Grellier, P., Bastin, P., and Kohl, L. (2009). Kinesin 9 family members perform separate functions in the trypanosome flagellum. J Cell Biol *187*, 615-622.
14. Duan, S., Li, H., Zhang, Y., Yang, S., Chen, Y., Qiu, B., Huang, C., Wang, J., Li, J., Zhu, X., *et al.* (2021). Rabl2 GTP hydrolysis licenses BBSome-mediated export to fine-tune ciliary signaling. EMBO J *40*, e105499.
15. Fliegauf, M., Benzing, T., and Omran, H. (2007). When cilia go bad: cilia defects and ciliopathies. Nat Rev Mol Cell Biol *8*, 880-893.
16. Gadadhar, S., Alvarez Viar, G., Hansen, J.N., Gong, A., Kostarev, A., Ialy-Radio, C., Leboucher, S., Whitfield, M., Ziyyat, A., Touré, A., *et al.* (2021). Tubulin glycylation controls axonemal dynein activity, flagellar beat, and male fertility. Science *371*.
17. Gibbons, I.R. (1961). The relationship between the fine structure and direction of beat in gill cilia of a lamellibranch mollusc. J Biophys Biochem Cytol *11*, 179–205.
18. Goetz, S.C., and Anderson, K.V. (2010). The primary cilium: a signalling centre during vertebrate development. Nat Rev Genet *11*, 331-344.

19. Graser, S., Stierhof, Y.-D., Lavoie, S.b.B., Gassner, O.S., Lamla, S., Le Clech, M., and Nigg, E.A. (2007). Cep164, a novel centriole appendage protein required for primary cilium formation. The Journal of Cell Biology *179*, 321-330.
20. Guirao, B., Meunier, A., Mortaud, S., Aguilar, A., Corsi, J.M., Strehl, L., Hirota, Y., Desoeuvre, A., Boutin, C., Han, Y.G.*, et al.* (2010). Coupling between hydrodynamic forces and planar cell polarity orients mammalian motile cilia. Nat Cell Biol *12*, 341-350.
21. Guo, Y., Li, D., Zhang, S., Yang, Y., Liu, J.J., Wang, X., Liu, C., Milkie, D.E., Moore, R.P., Tulu, U.S.*, et al.* (2018). Visualizing Intracellular Organelle and Cytoskeletal Interactions at Nanoscale Resolution on Millisecond Timescales. Cell *175*, 1430-1442 e1417.
22. Han, L., Rao, Q., Yang, R., Wang, Y., Chai, P., Xiong, Y., and Zhang, K. (2022). Cryo-EM structure of an active central apparatus. Nat Struct Mol Biol *29*, 472-482.
23. Herawati, E., Taniguchi, D., Kanoh, H., Tateishi, K., Ishihara, S., and Tsukita, S. (2016). Multiciliated cell basal bodies align in stereotypical patterns coordinated by the apical cytoskeleton. J Cell Biol *214*, 571-586.
24. Hirokawa, N., Noda, Y., Tanaka, Y., and Niwa, S. (2009). Kinesin superfamily motor proteins and intracellular transport. Nat Rev Mol Cell Biol *10*, 682-696.
25. Hoek, H., Klena, N., Jordan, M., Viar, G., Righetto, R., Schaffer, M., Erdmann, P., Wan, W., Geimer, S., Plitzko, J.*, et al.* (2022). In situ architecture of the ciliary base reveals the stepwise assembly of intraflagellar transport trains. Science *377*, 543–548
26. Inglis, P.N., Ou, G., Leroux, M.R., and Scholey, J.M. (2007). The sensory cilia of Caenorhabditis elegans. WormBook, 1-22.
27. Jordan, M.A., Diener, D.R., Stepanek, L., and Pigino, G. (2018). The cryo-EM structure of intraflagellar transport trains reveals how dynein is inactivated to ensure unidirectional anterograde movement in cilia. Nat Cell Biol *20*, 1250-1255.
28. Joung, J., Konermann, S., Gootenberg, J.S., Abudayyeh, O.O., Platt, R.J., Brigham, M.D., Sanjana, N.E., and Zhang, F. (2017). Genome-scale CRISPR-Cas9 knockout and transcriptional activation screening. Nat Protoc *12*, 828-863.
29. Kanie, T., Abbott, K.L., Mooney, N.A., Plowey, E.D., Demeter, J., and Jackson, P.K. (2017). The CEP19-RABL2 GTPase Complex Binds IFT-B to Initiate Intraflagellar Transport at the Ciliary Base. Dev Cell *42*, 22-36 e12.
30. Klena, N., and Pigino, G. (2022). Structural Biology of Cilia and Intraflagellar Transport. Annu Rev Cell Dev Biol *38*, 103-123.
31. Konjikusic, M.J., Lee, C., Yue, Y., Shrestha, B.D., Nguimtsop, A.M., Horani, A., Brody, S., Prakash, V.N., Gray, R.S., Verhey, K.J.*, et al.* (2023). Kif9 is an active kinesin motor required for ciliary beating and proximodistal patterning of motile axonemes. J Cell Sci *136*.
32. Konjikusic, M.J., Yeetong, P., Boswell, C.W., Lee, C., Roberson, E.C., Ittiwut, R., Suphapeetiporn, K., Ciruna, B., Gurnett, C.A., Wallingford, J.B.*, et al.* (2018). Mutations in Kinesin family member 6 reveal specific role in ependymal cell ciliogenesis and human neurological development. PLoS Genet *14*, e1007817.
33. Lechtreck, K.F., Delmotte, P., Robinson, M.L., Sanderson, M.J., and Witman, G.B. (2008). Mutations in Hydin impair ciliary motility in mice. J Cell Biol *180*, 633-643.
34. Lechtreck, K.F., Sanderson, M.J., and Witman, G.B. (2009). High-speed digital imaging of ependymal cilia in the murine brain. Methods Cell Biol *91*, 255-264.
35. Lindemann, C.B., and Lesich, K.A. (2021). The many modes of flagellar and ciliary beating:

Insights from a physical analysis. Cytoskeleton (Hoboken) *78*, 36-51.
36. Liu, H., Zheng, J., Zhu, L., Xie, L., Chen, Y., Zhang, Y., Zhang, W., Yin, Y., Peng, C., Zhou, J.*, et al.* (2021). Wdr47, Camsaps, and Katanin cooperate to generate ciliary central microtubules. Nat Commun *12*, 5796.
37. Lukinavicius, G., Reymond, L., D'Este, E., Masharina, A., Gottfert, F., Ta, H., Guther, A., Fournier, M., Rizzo, S., Waldmann, H.*, et al.* (2014). Fluorogenic probes for live-cell imaging of the cytoskeleton. Nat Methods *11*, 731-733.
38. Marshall, W.F., and Kintner, C. (2008). Cilia orientation and the fluid mechanics of development. Curr Opin Cell Biol *20*, 48-52.
39. Matsuo, M., Shimada, A., Koshida, S., Saga, Y., and Takeda, H. (2013). The establishment of rotational polarity in the airway and ependymal cilia: analysis with a novel cilium motility mutant mouse. Am J Physiol Lung Cell Mol Physiol *304*, L736-745.
40. Meleppattu, S., Zhou, H., Dai, J., Gui, M., and Brown, A. (2022). Mechanism of IFT-A polymerization into trains for ciliary transport. Cell *185*, 4986-4998 e4912.
41. Meng, Z., Meng, Q., Gao, T., Zhou, H., Xue, J., Li, H., Wu, Y., and Lv, J. (2022). Identification of bi-allelic KIF9 loss-of-function variants contributing to asthenospermia and male infertility in two Chinese families. Front Endocrinol (Lausanne) *13*, 1091107.
42. Miki, H., Okada, Y., and Hirokawa, N. (2005). Analysis of the kinesin superfamily: insights into structure and function. Trends Cell Biol *15*, 467-476.
43. Mirzadeh, Z., Han, Y.G., Soriano-Navarro, M., Garcia-Verdugo, J.M., and Alvarez-Buylla, A. (2010). Cilia organize ependymal planar polarity. J Neurosci *30*, 2600-2610.
44. Miyata, H., Shimada, K., Morohoshi, A., Oura, S., Matsumura, T., Xu, Z., Oyama, Y., and Ikawa, M. (2020). Testis-enriched kinesin KIF9 is important for progressive motility in mouse spermatozoa. FASEB J *34*, 5389-5400.
45. Mukherjee, K., and Brocchieri, L. (2013). Ancient Origin of Chaperonin Gene Paralogs Involved in Ciliopathies. J Phylogenetics Evol Biol *1*.
46. Nachury, M.V., and Mick, D.U. (2019). Establishing and regulating the composition of cilia for signal transduction. Nat Rev Mol Cell Biol *20*, 389-405.
47. Nguyen, Q.P.H., Liu, Z., Albulescu, A., Ouyang, H., Zlock, L., Coyaud, E., Laurent, E., Finkbeiner, W., Moraes, T.J., Raught, B.*, et al.* (2020). Comparative Super-Resolution Mapping of Basal Feet Reveals a Modular but Distinct Architecture in Primary and Motile Cilia. Dev Cell *55*, 209-223 e207.
48. Ohata, S., and Alvarez-Buylla, A. (2016). Planar Organization of Multiciliated Ependymal (E1) Cells in the Brain Ventricular Epithelium. Trends Neurosci *39*, 543-551.
49. Ohata, S., Nakatani, J., Herranz-Perez, V., Cheng, J., Belinson, H., Inubushi, T., Snider, W.D., Garcia-Verdugo, J.M., Wynshaw-Boris, A., and Alvarez-Buylla, A. (2014). Loss of Dishevelleds disrupts planar polarity in ependymal motile cilia and results in hydrocephalus. Neuron *83*, 558-571.
50. Pazour, G.J., Wilkerson, C.G., and Witman, G.B. (1998). A Dynein Light Chain Is Essential for the Retrograde Particle Movement of Intraflagellar Transport (IFT). J Cell Biol *141*, 979-992.
51. Pigino, G. (2021). Intraflagellar transport. Curr Biol *31*, R530-R536.
52. Portman, N., and Gull, K. (2010). The paraflagellar rod of kinetoplastid parasites: from structure to components and function. Int J Parasitol *40*, 135-148.
53. Qiao, C., Li, D., Liu, Y., Zhang, S., Liu, K., Liu, C., Guo, Y., Jiang, T., Fang, C., Li, N.*, et al.*

(2022). Rationalized deep learning super-resolution microscopy for sustained live imaging of rapid subcellular processes. Nat Biotechnol.

54. Ryu, H., Lee, H., Lee, J., Noh, H., Shin, M., Kumar, V., Hong, S., Kim, J., and Park, S. (2021). The molecular dynamics of subdistal appendages in multi-ciliated cells. Nat Commun *12*, 612.
55. Scholey, J.M. (2013). Kinesin-2: a family of heterotrimeric and homodimeric motors with diverse intracellular transport functions. Annu Rev Cell Dev Biol *29*, 443-469.
56. Siller, S.S., Sharma, H., Li, S., Yang, J., Zhang, Y., Holtzman, M.J., Winuthayanon, W., Colognato, H., Holdener, B.C., Li, F.Q.*, et al.* (2017). Conditional knockout mice for the distal appendage protein CEP164 reveal its essential roles in airway multiciliated cell differentiation. PLoS Genet *13*, e1007128.
57. Spassky, N., Merkle, F.T., Flames, N., Tramontin, A.D., Garcia-Verdugo, J.M., and Alvarez-Buylla, A. (2005). Adult ependymal cells are postmitotic and are derived from radial glial cells during embryogenesis. J Neurosci *25*, 10-18.
58. Taschner, M., Kotsis, F., Braeuer, P., Kuehn, E.W., and Lorentzen, E. (2014). Crystal structures of IFT70/52 and IFT52/46 provide insight into intraflagellar transport B core complex assembly. J Cell Biol *207*, 269-282.
59. Taschner, M., Weber, K., Mourao, A., Vetter, M., Awasthi, M., Stiegler, M., Bhogaraju, S., and Lorentzen, E. (2016). Intraflagellar transport proteins 172, 80, 57, 54, 38, and 20 form a stable tubulin-binding IFT-B2 complex. EMBO J *35*, 773-790.
60. Tissir, F., Qu, Y., Montcouquiol, M., Zhou, L., Komatsu, K., Shi, D., Fujimori, T., Labeau, J., Tyteca, D., Courtoy, P.*, et al.* (2010). Lack of cadherins Celsr2 and Celsr3 impairs ependymal ciliogenesis, leading to fatal hydrocephalus. Nat Neurosci *13*, 700-707.
61. Vincensini, L., Blisnick, T., and Bastin, P. (2011). 1001 model organisms to study cilia and flagella. Biol Cell *103*, 109-130.
62. Werner, M.E., Hwang, P., Huisman, F., Taborek, P., Yu, C.C., and Mitchell, B.J. (2011). Actin and microtubules drive differential aspects of planar cell polarity in multiciliated cells. J Cell Biol *195*, 19-26.
63. Williams, C.L., McIntyre, J.C., Norris, S.R., Jenkins, P.M., Zhang, L., Pei, Q., Verhey, K., and Martens, J.R. (2014). Direct evidence for BBSome-associated intraflagellar transport reveals distinct properties of native mammalian cilia. Nat Commun *5*, 5813.
64. Wingfield, J.L., Mengoni, I., Bomberger, H., Jiang, Y.-Y., Walsh, J.D., Brown, J.M., Picariello, T., Cochran, D.A., Zhu, B., Pan, J.*, et al.* (2017). IFT trains in different stages of assembly queue at the ciliary base for consecutive release into the cilium. eLife *6*.
65. Xu, Y., Cao, J., Huang, S., Feng, D., Zhang, W., Zhu, X., and Yan, X. (2015). Characterization of tetratricopeptide repeat-containing proteins critical for cilia formation and function. PLoS One *10*, e0124378.
66. Yokoyama, R., O'Toole, E., Ghosh, S., and Mitchell, D.R. (2004). Regulation of flagellar dynein activity by a central pair kinesin. Proc Natl Acad Sci U S A *101*.
67. Zhang, J., Wang, H., Imhof, S., Zhou, X., Liao, S., Atanasov, I., Hui, W.H., Hill, K.L., and Zhou, Z.H. (2021). Structure of the trypanosome paraflagellar rod and insights into non-planar motility of eukaryotic cells. Cell Discovery *7*.
68. Zhao, C., Omori, Y., Brodowska, K., Kovach, P., and Malicki, J. (2012). Kinesin-2 family in vertebrate ciliogenesis. Proceedings of the National Academy of Sciences *109*, 2388-2393.
69. Zhao, H., Chen, Q., Li, F., Cui, L., Xie, L., Huang, Q., Liang, X., Zhou, J., Yan, X., and Zhu, X.

(2021). Fibrogranular materials function as organizers to ensure the fidelity of multiciliary assembly. Nat Commun *12*, 1273.

70. Zheng, J., Liu, H., Zhu, L., Chen, Y., Zhao, H., Zhang, W., Li, F., Xie, L., Yan, X., and Zhu, X. (2019). Microtubule-bundling protein Spef1 enables mammalian ciliary central apparatus formation. J Mol Cell Biol *11*, 67-77.

Fig.1

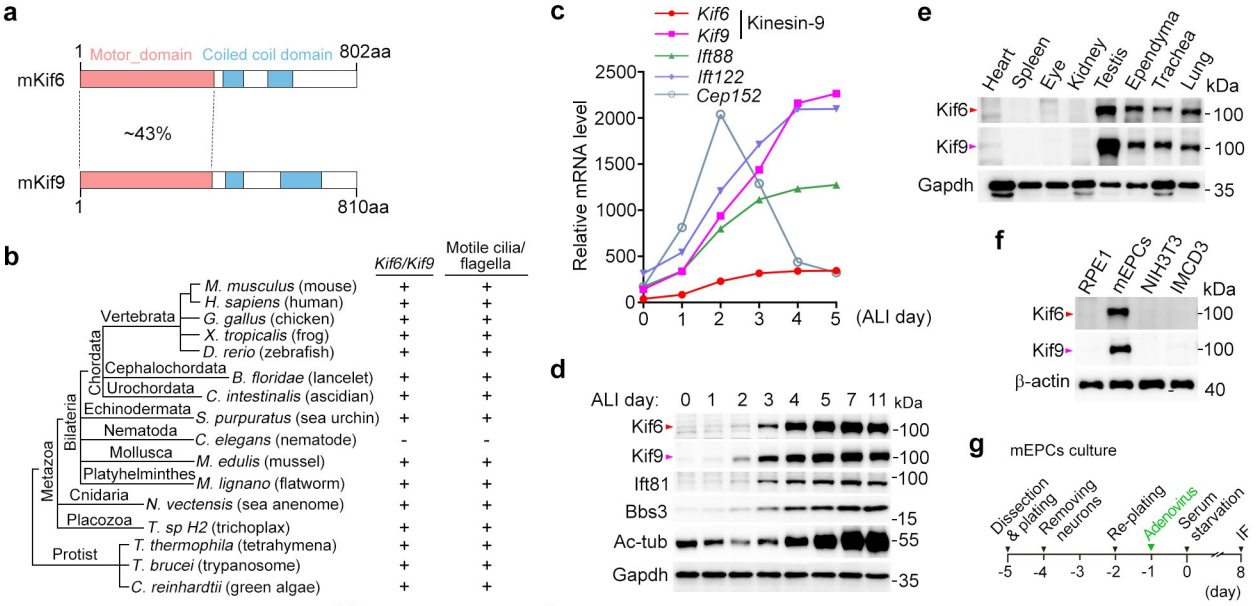
a
1 Motor_domain Coiled coil domain 802aa
mKif6
~43%
mKif9
1
810aa
b
Kif6/Kif9
Motile cilia/ flagella
Metazoa
Bilateria
Chordata
Vertebrata
M. musculus (mouse)
H. sapiens (human)
G. gallus (chicken)
X. tropicalis (frog)
D. rerio (zebrafish)
Cephalochordata
B. floridae (lancelet)
Urochordata
C. intestinalis (ascidian)
Echinodermata
S. purpuratus (sea urchin)
Nematoda
C. elegans (nematode)
Mollusca
M. edulis (mussel)
Platyhelminthes
M. lignano (flatworm)
Cnidaria
N. vectensis (sea anenome)
Placozoa
T. sp H2 (trichoplax)
Protist
T. thermophila (tetrahymena)
T. brucei (trypanosome)
C. reinhardtii (green algae)
c
Kif6
Kif9
Ift88
Ift122
Cep152
Kinesin-9
Relative mRNA level
(ALI day)
d
ALI day: 0 1 2 3 4 5 7 11 kDa
Kif6
Kif9
Ift81
Bbs3
Ac-tub
Gapdh
e
Heart Spleen Eye Kidney Testis Ependyma Trachea Lung
kDa
Kif6
Kif9
Gapdh
f
RPE1 mEPCs NIH3T3 IMCD3
kDa
Kif6
Kif9
β-actin
g
mEPCs culture
Dissection & plating
Removing neurons
Re-plating
Adenovirus
Serum starvation
(day)
h
mEPCs (day 8)
Ac-tub
Kif6
Kif6/Ac-tub
Kif9
Kif9/Ac-tub
5μm
i
IMCD3 (48h)
Ac-tub
Kif6
Ac-tub/Kif6/DAPI
Kif9
Ac-tub/Kif9/DAPI
2x
5μm
j
mEPCs (day 8)
Ac-tub
Kif6-GFP
Kif6-GFP/Ac-tub
Kif9-GFP
Kif9-GFP/Ac-tub
5μm
k
Hydin
Kif9
Ac-tub
Merge
2x
4μm
Relative intensity
Distance (μm)
l
Hydin
Kif6
Ac-tub
Merge
2x
4μm
Relative intensity
Distance (μm)

Fig. 2

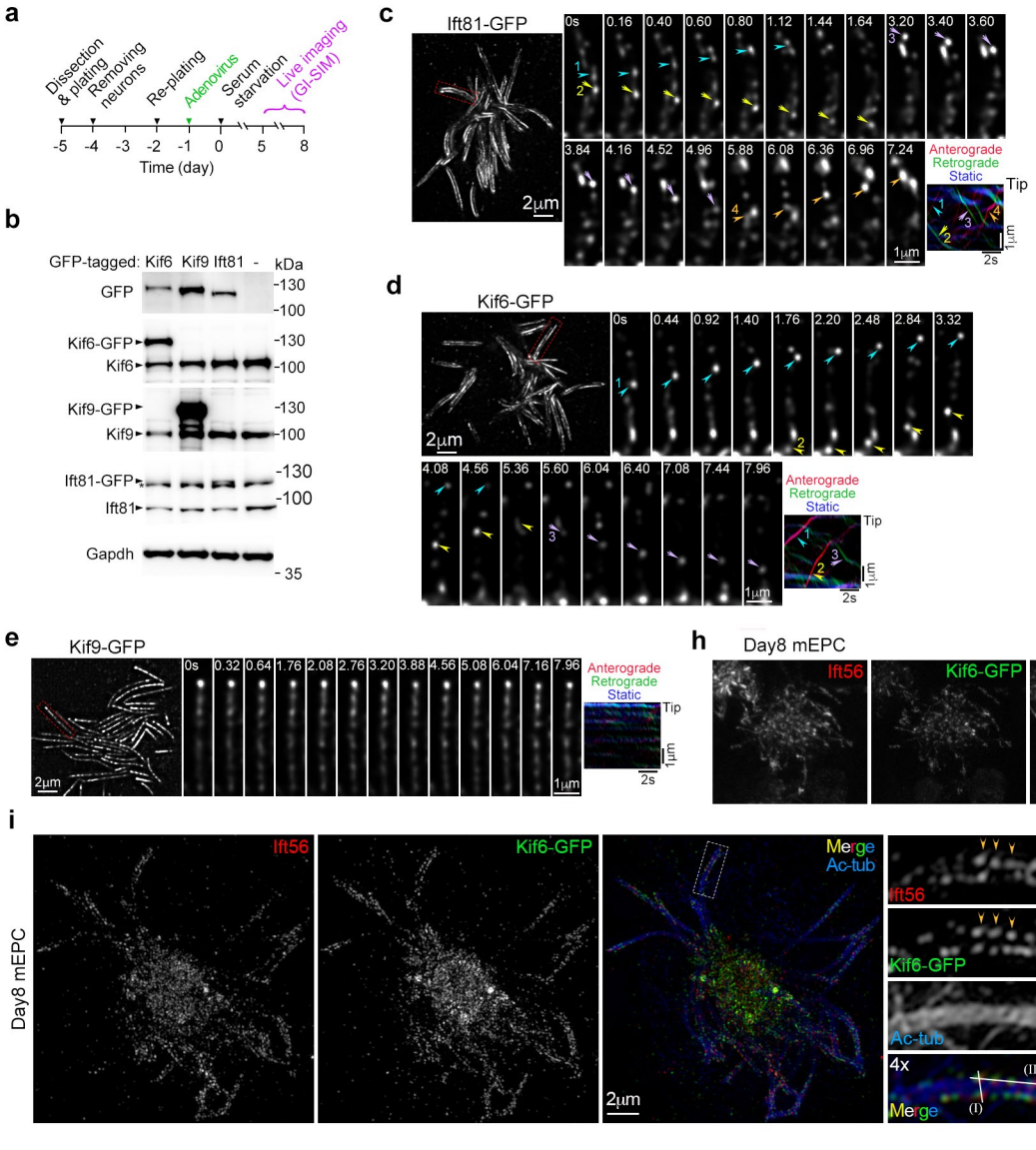
a
Dissection & plating
Removing neurons
Re-plating
Adenovirus
Serum starvation
Live imaging (GI-SIM)
-5 -4 -3 -2 -1 0 5 8
Time (day)
b
GFP-tagged: Kif6 Kif9 Ift81 -
kDa
GFP
Kif6-GFP
Kif6
Kif9-GFP
Kif9
Ift81-GFP
Ift81
Gapdh
130
100
35
c
Ift81-GFP
2μm
Anterograde
Retrograde
Static
Tip
1μm
2s
d
Kif6-GFP
2μm
Anterograde
Retrograde
Static
Tip
1μm
2s
e
Kif9-GFP
2μm
Anterograde
Retrograde
Static
Tip
1μm
2s
f
n=309 270 297 221
P=0.53
P=0.37
Velocity of ciliary GFP puncta (μm/s)
Ift81
Kif6
Antero
Retro
g
Cilia=165 153 165 153
P=0.55
P=0.0394
Frequency of GFP puncta in cilia (counts/min)
Ift81
Kif6
Antero
Retro
h
Day8 mEPC
Ift56
Kif6-GFP
Ac-tub
Merge
5μm
i
Day8 mEPC
Ift56
Kif6-GFP
Merge
Ac-tub
2μm
4x
Relative intensity
Distance (μm)

Fig. 3

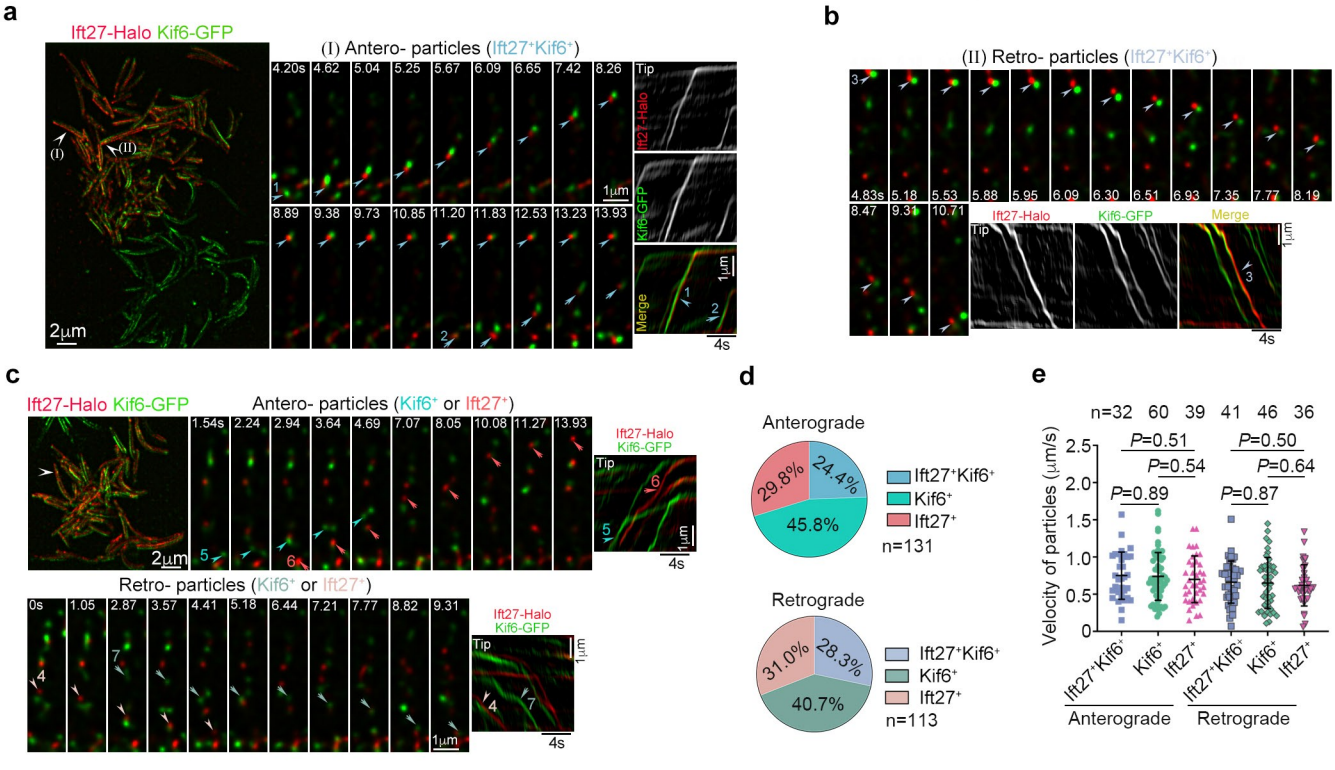
a
Ift27-Halo Kif6-GFP
(I) Antero- particles (Ift27⁺Kif6⁺)
(I)
(II)
2μm
4.20s 4.62 5.04 5.25 5.67 6.09 6.65 7.42 8.26
8.89 9.38 9.73 10.85 11.20 11.83 12.53 13.23 13.93
Tip
Ift27-Halo
Kif6-GFP
Merge
1μm
4s
b
(II) Retro- particles (Ift27⁺Kif6⁺)
4.83s 5.18 5.53 5.88 5.95 6.09 6.30 6.51 6.93 7.35 7.77 8.19
8.47 9.31 10.71
Ift27-Halo
Kif6-GFP
Merge
Tip
1μm
4s
c
Ift27-Halo Kif6-GFP
Antero- particles (Kif6⁺ or Ift27⁺)
1.54s 2.24 2.94 3.64 4.69 7.07 8.05 10.08 11.27 13.93
2μm
Ift27-Halo
Kif6-GFP
Tip
1μm
4s
Retro- particles (Kif6⁺ or Ift27⁺)
0s 1.05 2.87 3.57 4.41 5.18 6.44 7.21 7.77 8.82 9.31
1μm
d
Anterograde
24.4%
29.8%
45.8%
Ift27⁺Kif6⁺
Kif6⁺
Ift27⁺
n=131
Retrograde
28.3%
31.0%
40.7%
Ift27⁺Kif6⁺
Kif6⁺
Ift27⁺
n=113
e
n=32 60 39 41 46 36
P=0.51
P=0.54
P=0.89
P=0.50
P=0.64
P=0.87
Velocity of particles (μm/s)
2.5
2.0
1.5
1.0
0.5
0
Ift27⁺Kif6⁺
Kif6⁺
Ift27⁺
Ift27⁺Kif6⁺
Kif6⁺
Ift27⁺
Anterograde
Retrograde

Fig. 4

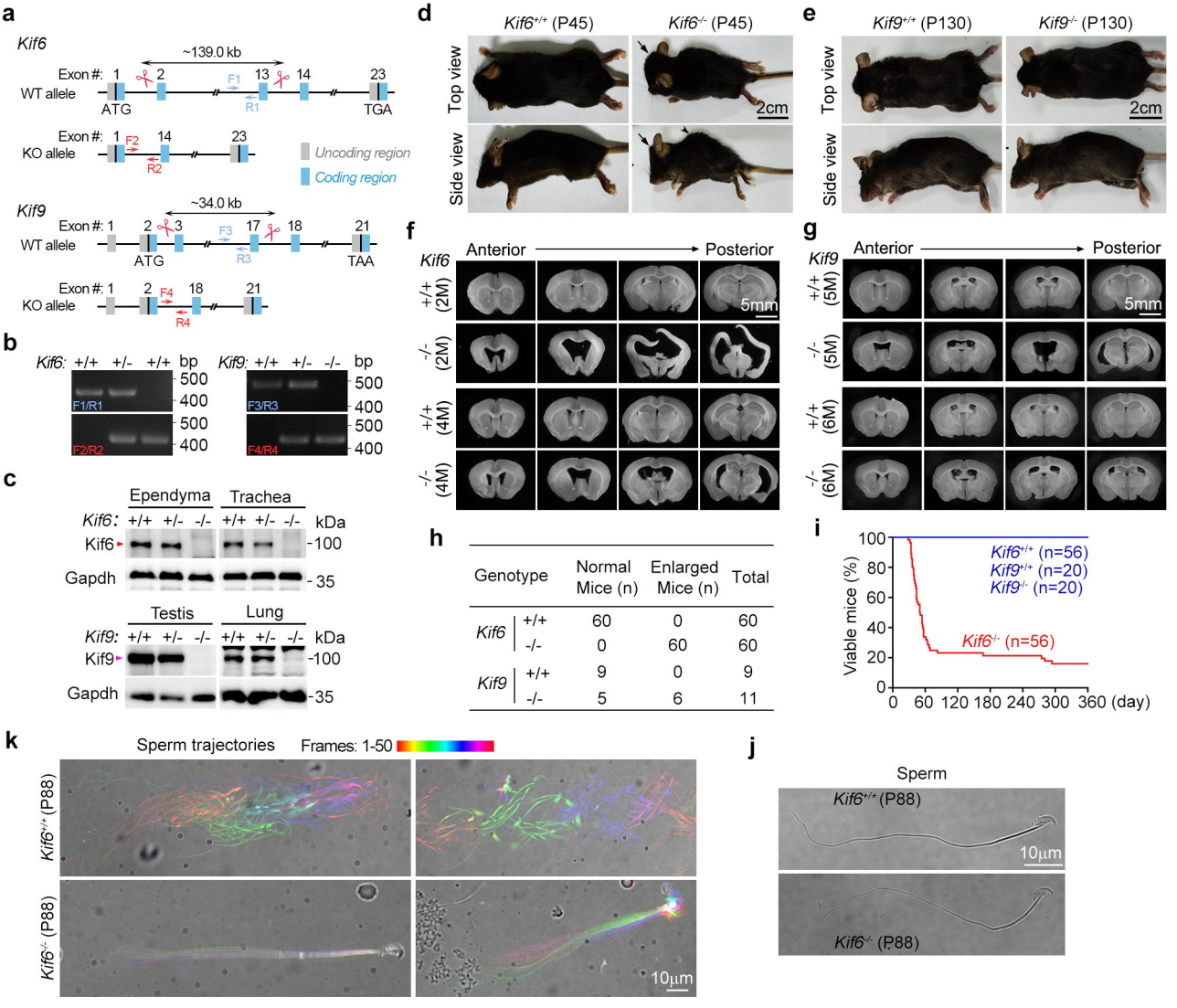

Genotype		Normal Mice (n)	Enlarged Mice (n)	Total
Kif6	+/+	60	0	60
	-/-	0	60	60
Kif9	+/+	9	0	9
	-/-	5	6	11

Fig. 5

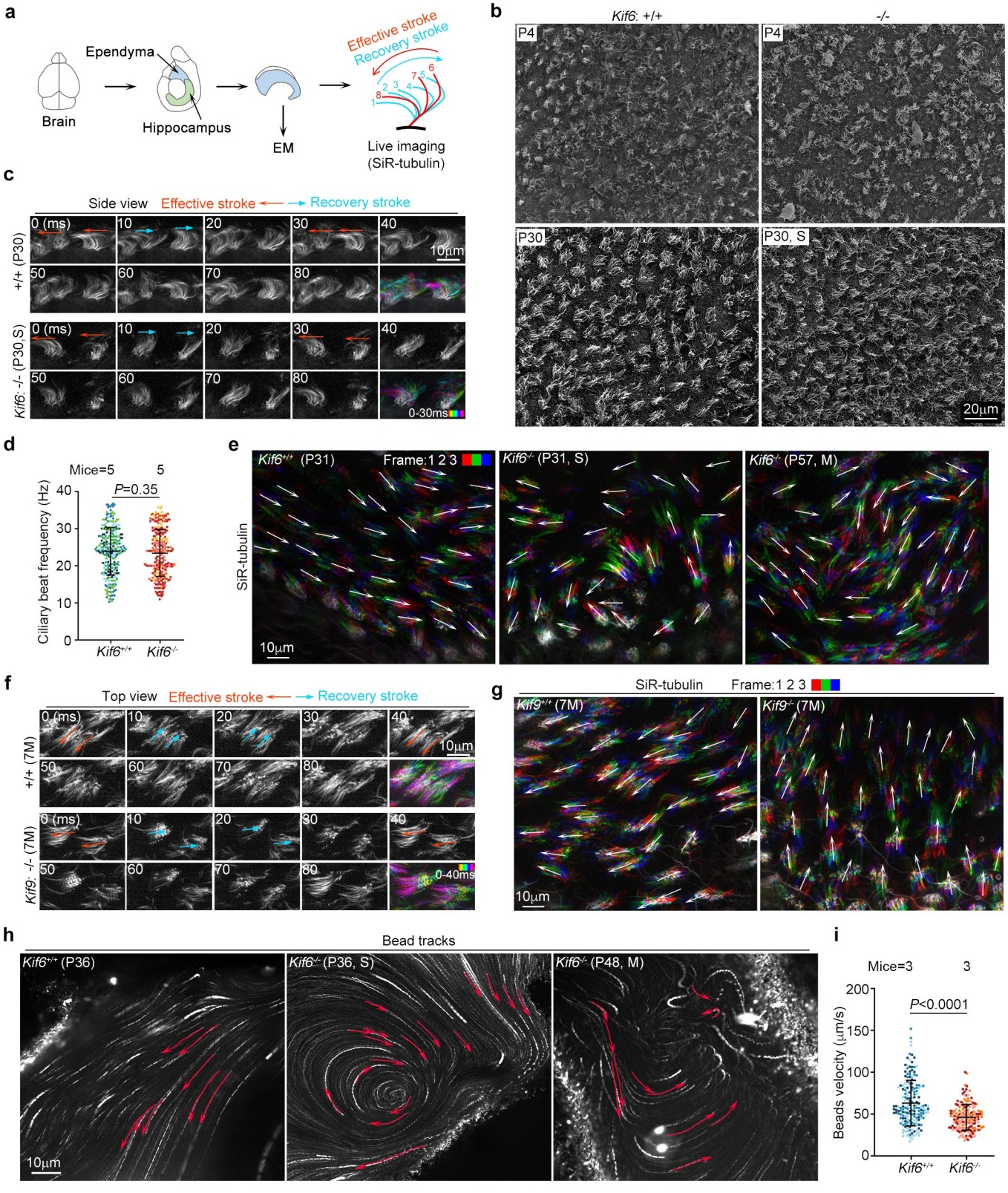
a
Ependyma
Brain
Hippocampus
EM
Effective stroke
Recovery stroke
Live imaging
(SiR-tubulin)
b
Kif6: +/+
-/-
P4
P4
P30
P30, S
20μm
c
Side view
Effective stroke
Recovery stroke
+/+ (P30)
Kif6: -/- (P30,S)
0 (ms)
10
20
30
40
50
60
70
80
10μm
0-30ms
d
Mice=5
5
P=0.35
Ciliary beat frequency (Hz)
Kif6+/+
Kif6-/-
e
Kif6+/+ (P31)
Frame:1 2 3
Kif6-/- (P31, S)
Kif6-/- (P57, M)
SiR-tubulin
10μm
f
Top view
Effective stroke
Recovery stroke
+/+ (7M)
Kif9: -/- (7M)
0-40ms
g
SiR-tubulin
Frame:1 2 3
Kif9+/+ (7M)
Kif9-/- (7M)
10μm
h
Bead tracks
Kif6+/+ (P36)
Kif6-/- (P36, S)
Kif6-/- (P48, M)
10μm
i
Mice=3
3
P<0.0001
Beads velocity (μm/s)
Kif6+/+
Kif6-/-

Fig. 6

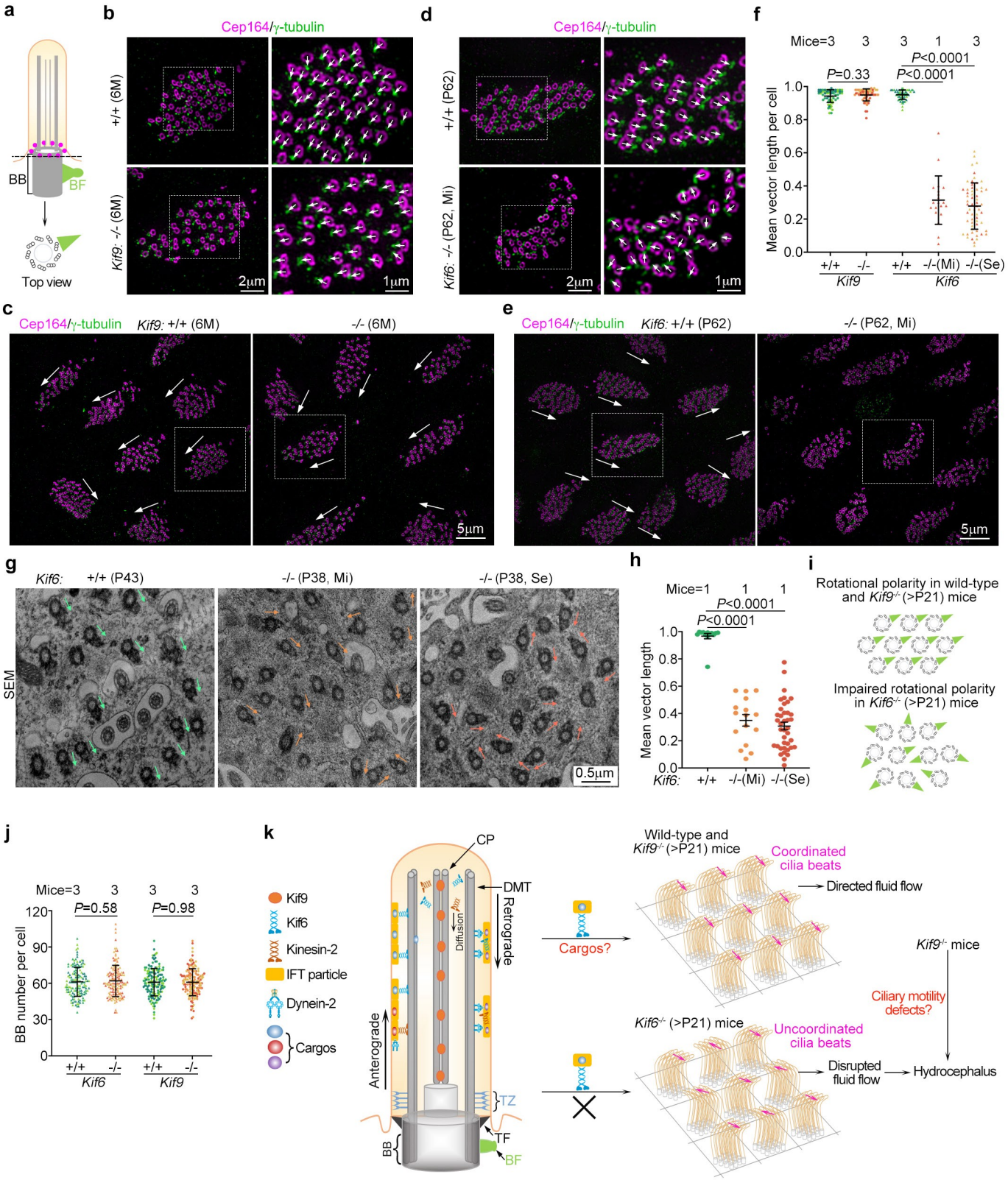
a
BB
BF
Top view
b
Cep164/γ-tubulin
+/+ (6M)
Kif9: -/- (6M)
2μm
1μm
d
Cep164/γ-tubulin
+/+ (P62)
Kif6: -/- (P62, Mi)
2μm
1μm
f
Mice=3 3 3 1 3
P=0.33
P<0.0001
P<0.0001
Mean vector length per cell
1.0
0.8
0.6
0.4
0.2
0.0
+/+ -/- +/+ -/-(Mi) -/-(Se)
Kif9
Kif6
c
Cep164/γ-tubulin
Kif9: +/+ (6M)
-/- (6M)
5μm
e
Cep164/γ-tubulin
Kif6: +/+ (P62)
-/- (P62, Mi)
5μm
g
Kif6: +/+ (P43)
-/- (P38, Mi)
-/- (P38, Se)
SEM
0.5μm
h
Mice=1 1 1
P<0.0001
P<0.0001
Mean vector length
1.0
0.8
0.6
0.4
0.2
0.0
Kif6: +/+ -/-(Mi) -/-(Se)
i
Rotational polarity in wild-type and Kif9-/- (>P21) mice
Impaired rotational polarity in Kif6-/- (>P21) mice
j
Mice=3 3 3 3
P=0.58
P=0.98
BB number per cell
120
90
60
30
0
+/+ -/- +/+ -/-
Kif6
Kif9
k
Kif9
Kif6
Kinesin-2
IFT particle
Dynein-2
Cargos
CP
DMT
Retrograde
Diffusion
Anterograde
TZ
TF
BF
BB
Cargos?
Wild-type and Kif9-/- (>P21) mice
Coordinated cilia beats
Directed fluid flow
Kif9-/- mice
Ciliary motility defects?
Kif6-/- (>P21) mice
Uncoordinated cilia beats
Disrupted fluid flow
Hydrocephalus

Fig.S1

a

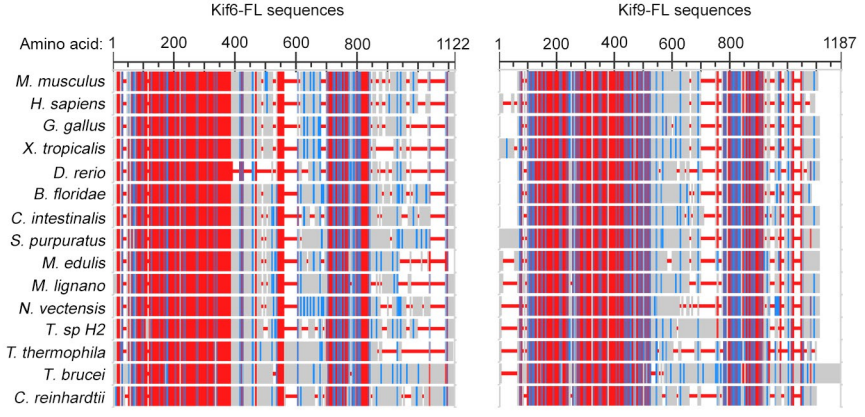

b

```
                                                  Motor domain                                  Amino acid
Kif6 KQTIQIFARVKPTVRKQQQGIYSIDEDEKLTHSLEIVLPRDLADGFVNNKRESYKFKFQRIFDQEAKQEIIFEIIAKPVA  80
Kif9 RKKVQAFVRVRPT---DDFAHEMIKYGED-NKSIDIHLKKDTRRGVVNNQQTDWSFKLDGVLHN-ASQDLVYETVAKDAV  75

     ESTLAGYNGTIFAYGQTGSGKTFTITGGAERYSDRGIIPRTLSYIFEQLQKDSSKIYTTHISYLEIYNECGYDLLDPRHE  160
     SQALDGYNGTIMCYGQTGAGKTYTMTGATENYKHRGILPRALQQVFRMIEERPTHAITVRVSYLEIYNENLFDLLSTLPY  155

     ASKLEDLPKVTILEDPDQNIHLKNLSLHQATTEEEALNLLFLGDTNRMIAETPMNQASTRSHCIFTVHLS--SKEPGSAT  238
     VGP--SVTPMTIVENP-QGIFIKGLSVHLTSQEEDAFSLLFEGETNRIIASHTMNKNSSRSHCIFTIYMEAHSRTLSDEK  232

     VRHAKLHLVDLAGSERVSKTGVGGLLLTEAKYINLSLHYLEQVIIALSEKHRTHIPYRNSMMTSVLRDSLGGNCMTTMIA  318
     YITSKINLVDLAGSERLSKTGSEGRVLKEATYINKSLSFLEQAIIALGDQNRDHVPFRQSKLTHALKDSLGGNCNMVLVT  312

     TLSLEKRNIDESISTCRFAQRVALIKNEAILNE  351
     NIYGEAAQLDETLSSLRFASRMKLVTTEPAINE  345
```

Fig.S2

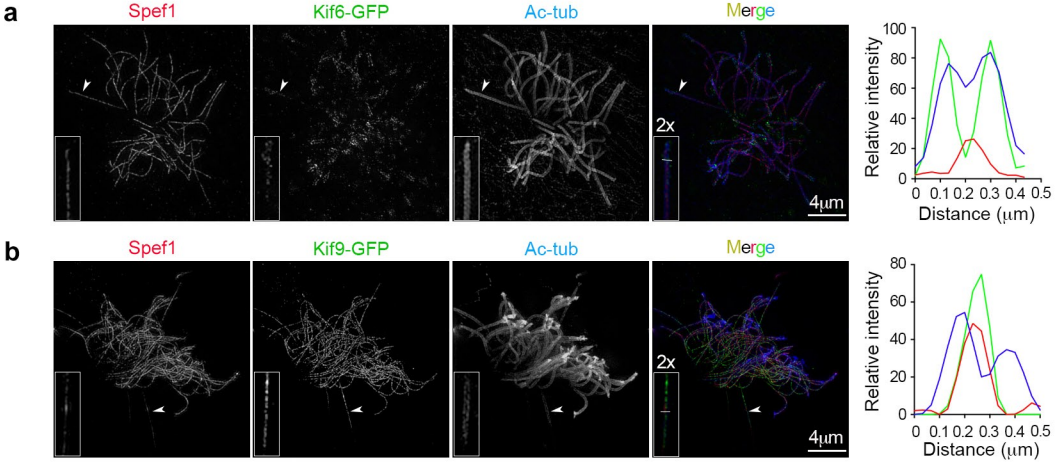
a
Spef1
Kif6-GFP
Ac-tub
Merge
2x
4μm
Relative intensity
100
80
60
40
20
0
0 0.1 0.2 0.3 0.4 0.5
Distance (μm)
b
Spef1
Kif9-GFP
Ac-tub
Merge
2x
4μm
Relative intensity
80
60
40
20
0
0 0.1 0.2 0.3 0.4 0.5
Distance (μm)

Fig. S3

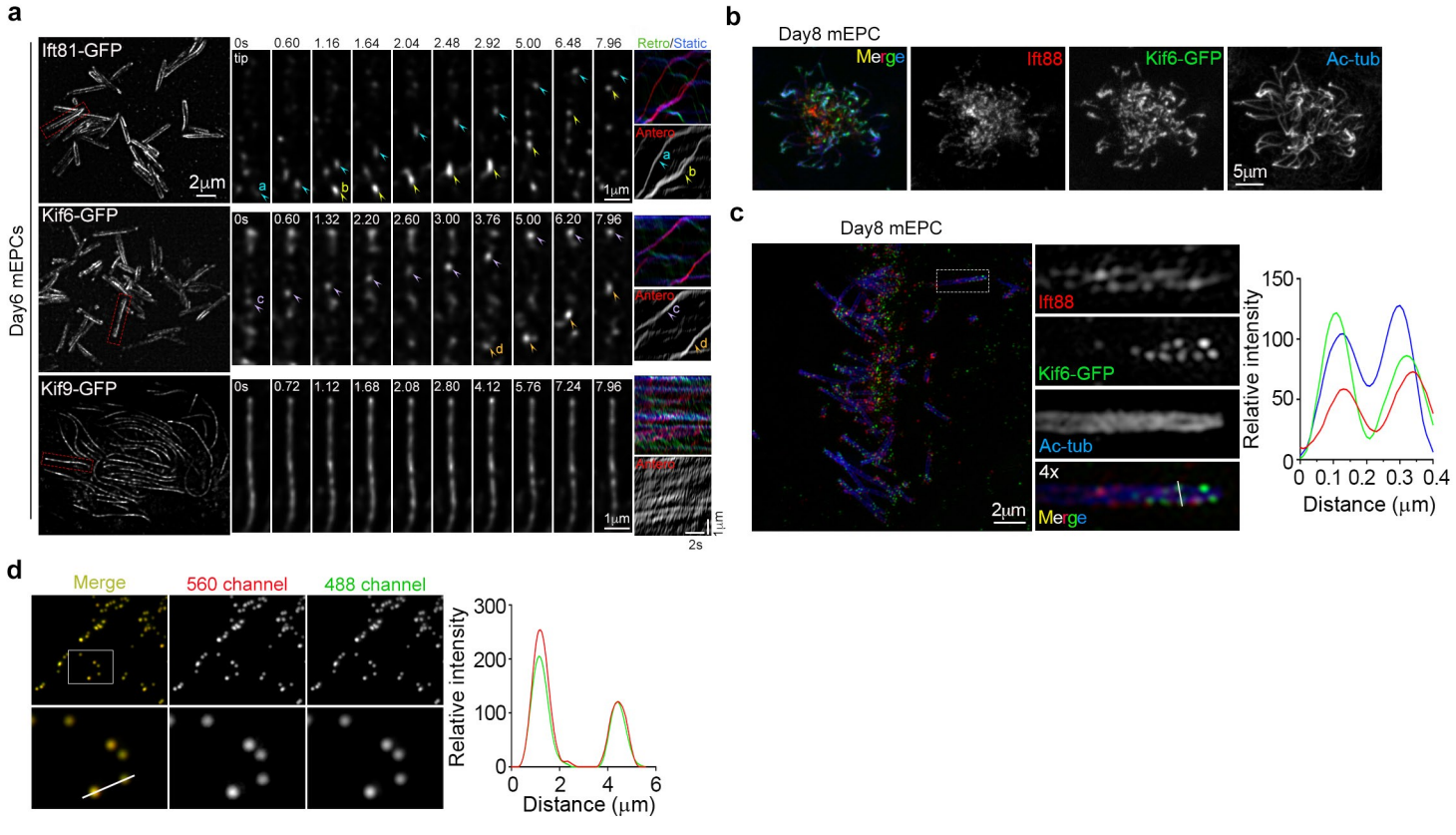
a
Day6 mEPCs
Ift81-GFP
Kif6-GFP
Kif9-GFP
2μm
tip
0s 0.60 1.16 1.64 2.04 2.48 2.92 5.00 6.48 7.96
0s 0.60 1.32 2.20 2.60 3.00 3.76 5.00 6.20 7.96
0s 0.72 1.12 1.68 2.08 2.80 4.12 5.76 7.24 7.96
Retro/Static
Antero
1μm
2s
b
Day8 mEPC
Merge
Ift88
Kif6-GFP
Ac-tub
5μm
c
Day8 mEPC
2μm
Ift88
Kif6-GFP
Ac-tub
4x
Merge
Relative intensity
Distance (μm)
d
Merge
560 channel
488 channel
Relative intensity
Distance (μm)

Fig. S4

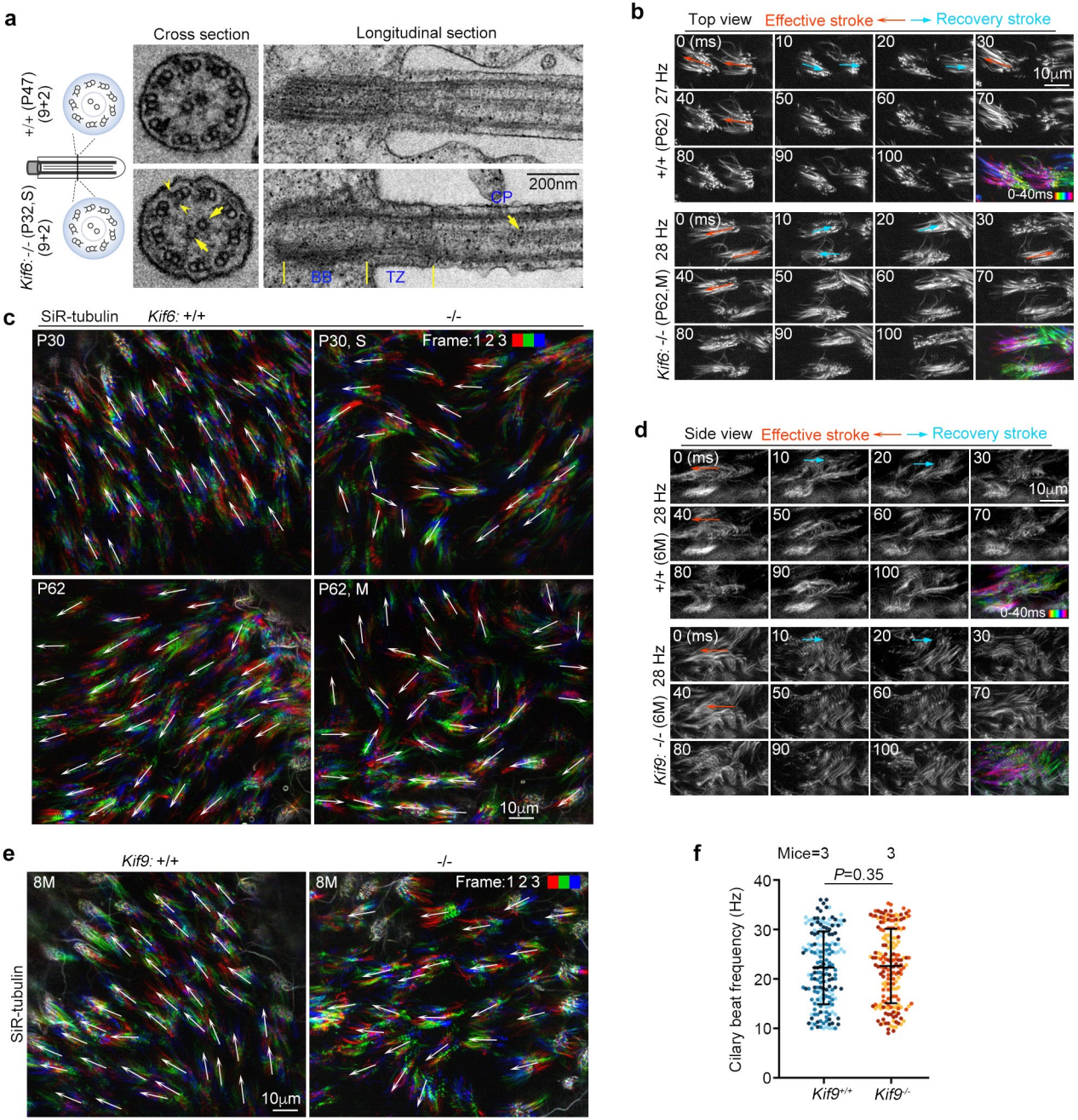
a
Cross section
Longitudinal section
+/+ (P47) (9+2)
Kif6: -/- (P32,S) (9+2)
200nm
CP
BB
TZ
b
Top view
Effective stroke
Recovery stroke
0 (ms)
10
20
30
10μm
40
50
60
70
80
90
100
0-40ms
27 Hz
+/+ (P62)
28 Hz
(P62,M)
Kif6: -/- (P62,M)
c
SiR-tubulin
Kif6: +/+
-/-
P30
P30, S
Frame:1 2 3
P62
P62, M
10μm
d
Side view
Effective stroke
Recovery stroke
28 Hz
+/+ (6M)
Kif9: -/- (6M)
e
Kif9: +/+
-/-
8M
SiR-tubulin
f
Mice=3
3
P=0.35
Cilary beat frequency (Hz)
Kif9+/+
Kif9-/-

Fig. S5

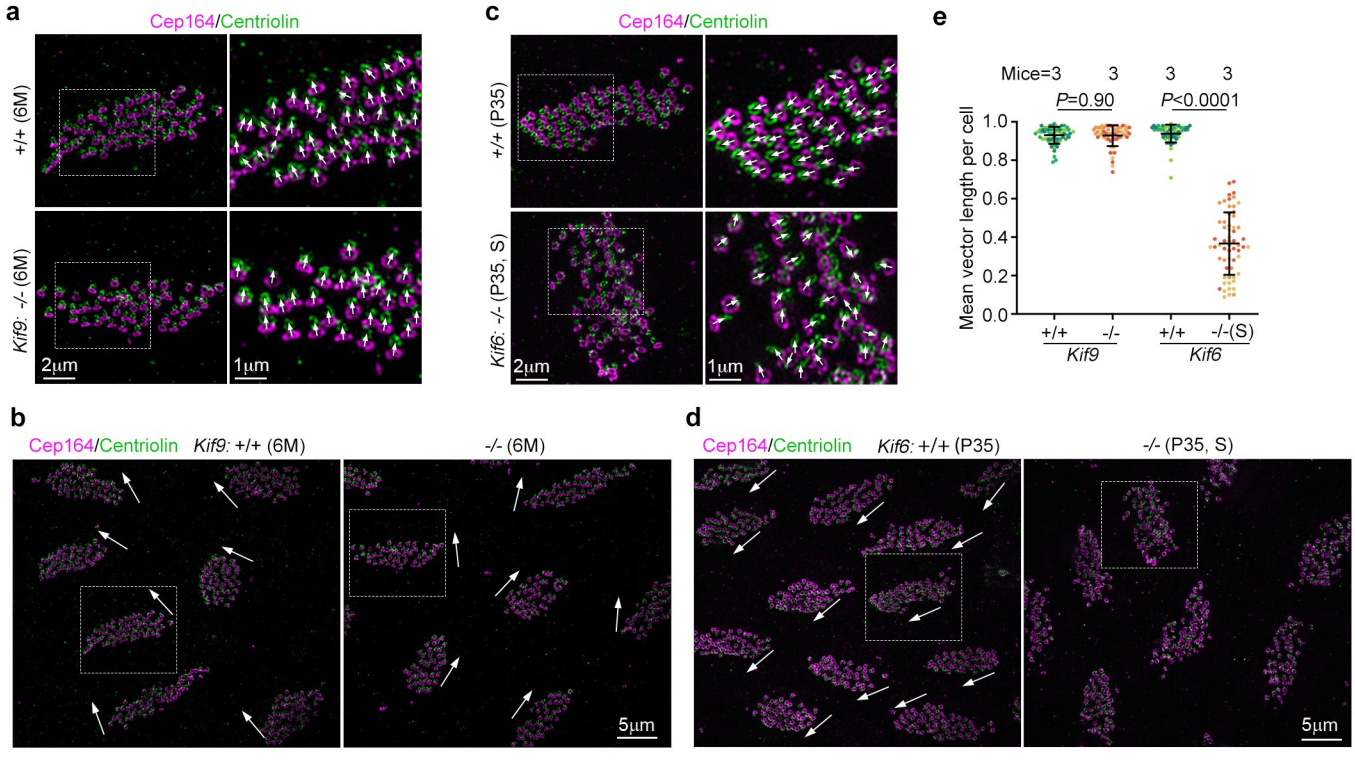
a
Cep164/Centriolin
+/+ (6M)
Kif9: -/- (6M)
2μm
1μm
c
Cep164/Centriolin
+/+ (P35)
Kif6: -/- (P35, S)
2μm
1μm
e
Mice=3 3 3 3
P=0.90
P<0.0001
Mean vector length per cell
1.0
0.8
0.6
0.4
0.2
0.0
+/+
-/-
+/+
-/-(S)
Kif9
Kif6
b
Cep164/Centriolin
Kif9: +/+ (6M)
-/- (6M)
5μm
d
Cep164/Centriolin
Kif6: +/+ (P35)
-/- (P35, S)
5μm

Fig. S6

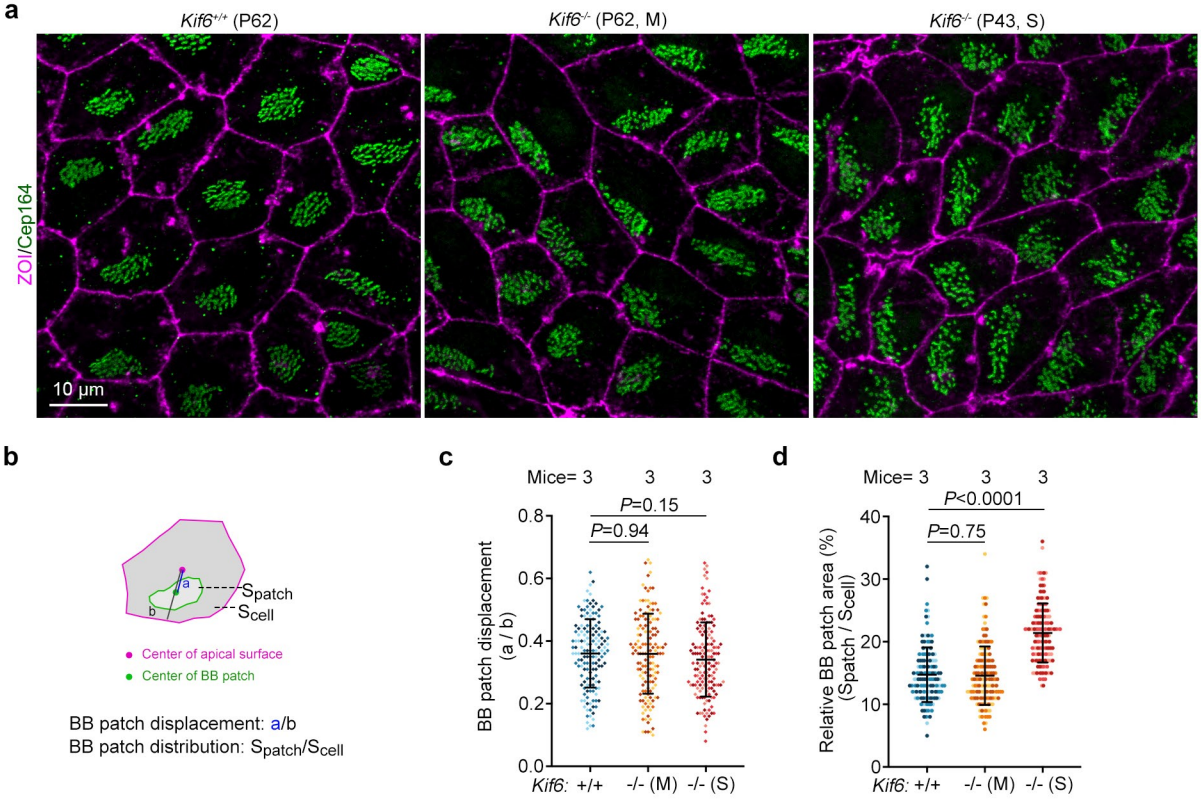
a
Kif6+/+ (P62)
Kif6-/- (P62, M)
Kif6-/- (P43, S)
ZO1/Cep164
10 μm
b
a
b
Spatch
Scell
Center of apical surface
Center of BB patch
BB patch displacement: a/b
BB patch distribution: Spatch/Scell
c
Mice= 3 3 3
P=0.15
P=0.94
BB patch displacement (a / b)
0.0
0.2
0.4
0.6
0.8
Kif6: +/+ -/- (M) -/- (S)
d
Mice= 3 3 3
P<0.0001
P=0.75
Relative BB patch area (%) (Spatch / Scell)
0
10
20
30
40
Kif6: +/+ -/- (M) -/- (S)